*International Geology Review*, Vol. 49, 2007, p. 658–679.
Copyright © 2007 by V. H. Winston & Son, Inc. All rights reserved.

# Transformation of Subcontinental Lithospheric Mantle through Peridotite-Melt Reaction: Evidence from a Highly Fertile Mantle Xenolith from the North China Craton

HONG-FU ZHANG,[1]

*State Key Laboratory of Lithospheric Evolution, Institute of Geology and Geophysics, Chinese Academy of Sciences, P.O. Box 9825, Beijing 100029, China*

EIZO NAKAMURA,

*The Pheasant Memorial Laboratory for Geochemistry and Cosmochemistry, Institute for Study of the Earth's Interior, Okayama University at Misasa, Tottori 682-0193, Japan*

MIN SUN,

*Department of Earth Sciences, The University of Hong Kong, Pokfulam Road, Hong Kong*

KATSURA KOBAYASHI,

*The Pheasant Memorial Laboratory for Geochemistry and Cosmochemistry, Institute for Study of the Earth's Interior, Okayama University at Misasa, Tottori 682-0193, Japan*

JIN ZHANG, JI-FENG YING, YAN-JIE TANG, AND LI-FENG NIU

*State Key Laboratory of Lithospheric Evolution, Institute of Geology and Geophysics, Chinese Academy of Sciences, P.O. Box 9825, Beijing 100029, China*

## Abstract

A highly fertile mantle xenolith entrained in the Upper Cretaceous Daxizhuang basalt, Shandong Province, China provides petrological evidence for reaction between basaltic melt and refractory peridotite in Mesozoic lithospheric mantle beneath the eastern North China craton. The xenolith is zoned with a lherzolite core, a sheared wehrlite mantle, and a reactant rim. The lherzolite has a medium-grained granular texture and contains olivine, orthopyroxene, clinopyroxene, and spinel with low Mg# values (≤87). This is the lowest value observed globally in mantle xenoliths entrained in both kimberlites and basalts from old cratons, but is close to low-Mg# spinel lherzolites entrained in adjacent region of the eastern North China craton. The wehrlite mantle shows clear orientation and foliation of constituent olivine and clinopyroxene. The reactant rim displays a symplectite texture of fine-grained olivine, clinopyroxene, and spinel, and is characterized by LREE-enriched patterns. Orthopyroxene is lacking from the sheared mantle and reactant rim. Clear zoning and systematic core-rim variations in major and trace elements of the constituent minerals demonstrate the occurrence of the refertilization through the melt-peridotite reaction in the xenolith. This reaction may have produced the low-Mg# peridotite from a high-Mg# protolith and could be an important mechanism for the change of the subcontinental lithospheric mantle from a Paleozoic refractory mantle to a Late Mesozoic fertile mantle.

## Introduction

THE TERM "craton" refers to tectonically stable continents formed in early Earth history, as evidenced by the existence of Archean basement (Jordan, 1975, 1988). Kimberlites of the Kaapvaal craton, South Africa, contain a large number of mantle xenoliths, and thus provide excellent samples for study of the continental lithospheric mantle. These xenoliths are depleted in incompatible elements such as large-ion lithophile elements (LILE), and are refractory as indicated by their high Mg# numbers. Re-Os isotopic data for these xenoliths yield old ages similar to the regional Archean crust (Pearson et al., 1995; Pearson, 1999). These results support suggestions that the primordial crust formed

[1]Corresponding author; email: hfzhang@mail.igcas.ac.cn

by extraction of high-degree partial melts from the bulk-silicate Earth mantle, and the residue became the refractory lithosphere (Jordan, 1975, 1988). Therefore, it is envisaged that in cratonic regions, Archean crust overlies lithospheric mantle composed of old, highly refractory spinel- to diamond-facies peridotites (Richardson et al., 1984, 1985). The cratonic lithospheric mantle is buoyant due to extensive removal of basaltic components (e.g., alkalis, CaO, FeO, and $Al_2O_3$). This physical property allows the cratonic crust and its lithospheric keel to remain tectonically intact for billions of years, effectively isolating the conductive lithosphere from convective asthenosphere (Boyd, 1989; Boyd et al., 1997). However, recent studies show that some cratons may fail to maintain their lithospheric mantle stability over time. Destruction, modification, and reconstruction took place for example, underneath the western North American and Antarctic cratons (Lee et al., 2000; Zhang et al., 2001a; Riley et al., 2003).

This is more prominent for the North China craton (Fan and Menzies, 1992; Menzies et al., 1993; Griffin et al., 1998). Paleozoic kimberlite diatremes on the craton contain mantle xenoliths, xenocrysts, and diamond inclusions. Data from mantle xenoliths and mineral inclusions reveal that a thick, cold, refractory (Fo up to 93–94) lithospheric mantle of Archean age existed beneath this craton in the Paleozoic (Meyer et al., 1994; Harris et al., 1994; Chi and Lu, 1996; Zheng et al., 2001; Xu, 2001; Wang and Gasparik, 2001; Gao et al., 2002). However, peridotitic xenoliths from Cenozoic basalts give young ages and possessed an "oceanic" compositional affinity (Fan et al., 2000; Zheng et al., 2001; Gao et al., 2002; Wu et al., 2003). Recent studies demonstrate that a lithospheric thickness of more than 100 km was removed (Fan and Menzies, 1992; Menzies et al., 1993; Griffin et al., 1998). This dramatic lithospheric loss was accompanied by a compositional change from a refractory lithospheric mantle in the Paleozoic to a fertile mantle in the Cenozoic. Geochemical study of Mesozoic magmatism suggests that the compositional change was probably caused by an addition of crustal melts from circum-cratonic subducted slabs (Fan et al., 2001; Zhang et al., 2002, 2003b, 2004; Xu et al., 2004; Ying et al., 2004). Study of mantle olivine xenocrysts suggests that this compositional change was possibly due to peridotite-melt interaction (Zhang, 2005). However, more direct evidence for this process is still lacking.

A highly fertile peridotitic xenolith from the Mesozoic Daxizhuang basalt shows a deformation texture and a systematic compositional change from a lherzolite core to a wehrlite reactant rim. All minerals show chemical variation. The xenolith provides petrological evidence for transformation of subcontinental lithospheric mantle through peridotite-melt reaction. Decompressional melting of this highly modified lithospheric mantle in response to regional lithospheric extension may have caused removal of the cratonic lithospheric keel. This paper reports petrologic and geochemical data on this composite xenolith to constrain the nature and evolution of the Mesozoic lithospheric mantle.

## Geological Background

The North China craton is bounded to the south by the Qinling-Dabie-Sulu orogenic belt (Li et al., 1993; Meng and Zhang, 2000) and to the north by the Central Asian orogenic belt (Sengör et al., 1999) (Fig. 1A). The Qinling-Dabie-Sulu orogenic belt resulted from Triassic continental collision (Li et al., 1993). The occurrence of diamond and coesite in eclogites (Xu et al., 1992) and coesite inclusions in zircons from both ortho- and para-gneisses (Liu et al., 2001) all demonstrate that the upper and middle crustal units of the Yangtze block were once subducted to ultrahigh-pressure conditions. The subduction and subsequent collision significantly affected the lithospheric mantle beneath the southern North China craton. Melts from subducted crustal materials fertilized the overlying lithospheric mantle, as documented in Mesozoic lithosphere-derived basaltic rocks (Zhang et al., 2002, 2004; Zhang and Sun, 2002; Fan et al., 2004; Xu et al., 2004; Wang et al., 2005).

In the eastern North China craton, the Tan-Lu fault separates Shandong Province into two parts (Fig. 1B), the Jiaodong and Luxi regions. Mesozoic basaltic-trachyandesitic volcanic rocks and dioritic-granitoid intrusions are distributed in both areas (Fig. 1B), whereas mafic intrusions dominate the Luxi region. In Jiaodong, the Sulu ultrahigh-pressure metamorphic belt was traditionally regarded as the suture of the Triassic collision between the North China craton and Yangtze craton (Okay and Sengör, 1992; Yin and Nie, 1993). However, in recent years, more and more evidence supports a crustal-detachment model (Li, 1994; Chung, 1999). According to this model, the upper and middle crust of the Yangtze craton was detached

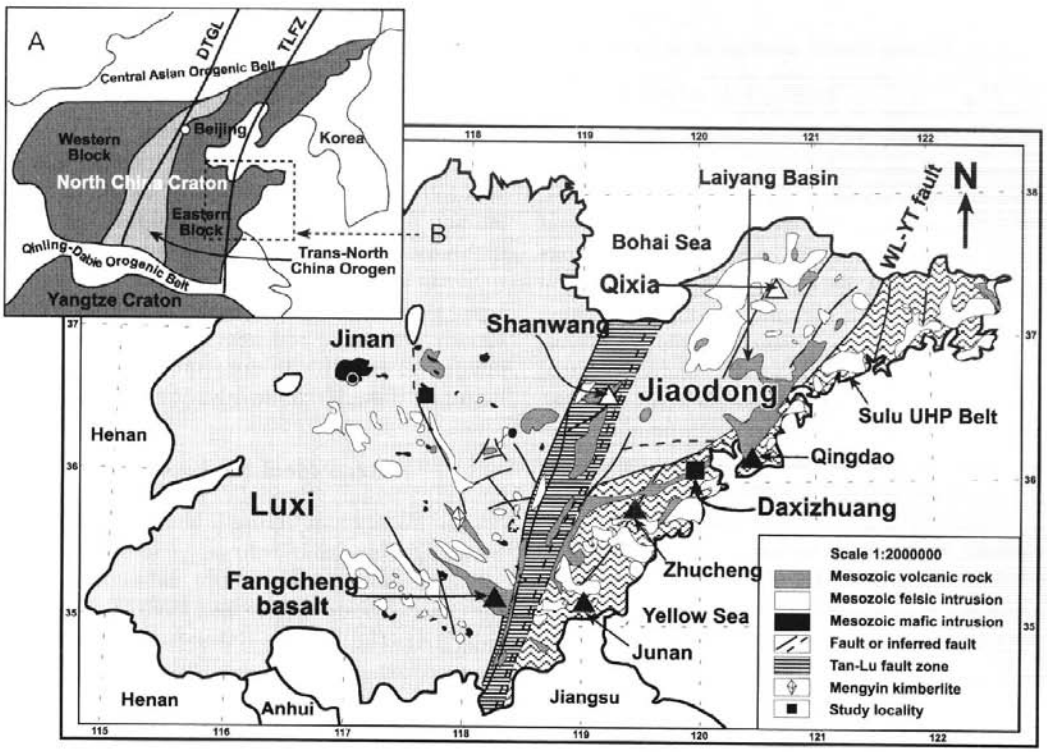



FIG. 1. A. Simplified geological map showing the major tectonic units of the North China craton (Zhao et al., 2001). The study area, Shangdong Province, is situated in the Eastern Block of the North China craton. B. Distribution of Mesozoic intrusive and volcanic rocks (after Zhang and Sun, 2002), as well as Paleozoic Mengyin diamondiferous kimberlite. The Tan-Lu fault zone (TLFZ) separates the Eastern Block into the Luxi and Jiaodong regions. Abbreviations: WL-YT fault = Wulian-Yantai fault. Solid square shows the localities of the Cretaceous xenolith- or xenocryst-bearing basaltic rocks in Shandong Province. Open triangle represents adjacent localities of the Cenozoic xenolith-bearing basalts (Zheng et al., 1998), which are used for comparison with this composite xenolith.

from its lower crust and thrust northward over the North China craton for about 400 km. Thus, the present Wulian-Yantai fault is just the surface boundary rather than the lithospheric boundary, which is far away from the suture near Nanjing, Jiangsu Province (Li, 1994). Consequently, the lower crust and lithospheric mantle beneath the Sulu metamorphic belt should be part of the North China craton.

Mesozoic volcanic rocks are widespread in extensional basins of the Sulu terrain (Fig. 1B). Mafic volcanic rocks include the Lower Cretaceous Qingshan Formation and the Upper Cretaceous Wangshi Group (LSGB, 1981). The Qingshan Formation is composed of calc-alkaline rocks (basalts, basaltic andesites, and trachyandesites) and locally contains bimodal basaltic and rhyolitic rocks (Fan et al., 2001). The volcanic units in the Wangshi Group are dominantly alkali basalts as represented by the Daxizhuang basalt (Yan et al., 2003). Basaltic rocks formed at 65–86 Ma also occurred as breccias or dikes, for example the Junan mafic volcanic breccia (Ying et al., 2006) and the Qingdao and Zhucheng lamprophyric dikes (Han and Fu, 1993) (Fig. 1B). All these Upper Cretaceous basaltic rocks contain mantle and lower-crustal xenoliths (peridotites, pyroxenites and granulites) and xenocrysts (olivines and pyroxenes). A composite xenolith was collected from the Daxizhuang basalt for this study. Two Cenozoic basalt localities (Fig. 1B)—Shanwang (within the Tan-Lu fault) and Qixia (distant from the fault)—were selected for comparison.

*Host basalt*

Daxizhuang basalts erupted at 73.5 Ma (Yan et al., 2003) are distributed within the Cretaceous Jiaolai Basin. They stratigraphically belong to the Upper Cretaceous Wangshi Group and are classified as alkali basalts with more than 6% normative nepheline. These basalts are lava flows, with olivine phenocrysts (8–15%) and matrix plagioclase and pyroxene. A geochemical study of the basalt has been conducted by Yan et al. (2003). Daxizhuang lavas contain abundant spinel-facies peridotitic xenoliths. The xenoliths are 3–10 cm in size and dominantly composed of granular olivine (60–70%), orthopyroxene (15–20%), and clinopyroxene (10–15%) with minor spinel; thus they are spinel lherzolites. The deformation texture ubiquitously occurs in olivine and orthopyroxene. Here we concentrate on a unique composite xenolith, which is highly fertile and has a sheared and zoned texture.

*The composite xenolith*

The xenolith (12 × 6 × 2 cm) comprises three different zones—a lherzolite core, a sheared mantle, and a reactant rim against the host basalt (Fig. 2). The lherzolite is composed of medium-grained granular olivine (58%), orthopyroxene (34%), clinopyroxene (6%), and spinel (2%). Grain sizes are dominantly in the range of 0.5–2 mm with few pyroxenes up to 3.5 mm (Fig. 2). Some clinopyroxenes in the lherzolite show sieve texture in the rim (Fig. 3C), i.e. serpentine or chlorite set within clinopyroxene crystals. The sheared mantle (Fig. 2) is a wehrlite dominantly composed of olivine (60%) and clinopyroxene (35%) with minor spinel, and is characterized by olivine orientation and foliation. No orthopyroxene exists in the sheared mantle. The orthopyroxene could have dissolved during the fluid/melt-assisted deformation. The clinopyroxene displays a darker chlorite core surrounded by a lighter clinopyroxene rim (Fig. 2). Similar to clinopyroxene in the lherzolite, the clinopyroxene in the sheared mantle also has a clean core and a sieve-texture rim (Fig. 3B). Serpentine/chlorite occurs ubiquitously along the cracks. The reactant rim in contact with the host basalt is also composed of fine-grained olivine (40%), clinopyroxene (35%), and spinel (25%). All the clinopyroxenes have a spongy and symplectite or sieve texture (Figs. 2 and 3A). Orthopyroxene does not occur in the reactant rim. All minerals in contact with the host basalt show a clear textural zonation with Fe-richer portions toward the basalt. The unusual clinopyroxene texture in this composite xenolith (Fig. 3) demonstrates involvement of a Cl-rich melt and/or fluid in the reaction.

## Analytical Methods

Major-element compositions of minerals were obtained with a Cameca SX50 EPMA at the State Key Laboratory of Lithospheric Evolution, Institute of Geology and Geophysics, Chinese Academy of Sciences. Analyses were performed with a beam of 15 KeV and 20 nA focused to a spot ~2 μm in diameter. The results are presented in Tables 1–4.

Trace element analyses of clinopyroxenes were carried out with the Cameca ims-5f ion microprobe at the Pheasant Memorial Laboratory for Geochemistry and Cosmochemistry, Institute for Study of the Earth's Interior, Okayama University at Misasa, following the procedures described in Nakamura and Kushiro (1998). Standard clinopyroxenes from mantle xenoliths and basaltic glasses were used for the calibration of trace element concentrations. These standards have been well characterized in terms of homogeneity and concentrations by both the ion microprobe and ICP-MS (Nakamura et al., 2003). In order to reduce the charge build-up, the polished thin sections were coated by 20 nm thick gold film.

Analytical reproducibilities (RSD 1σ% in $n$ = 10) for trace elements in the clinopyroxene and basaltic standard were typically ~5%. The trace element abundances in the analyzed materials were similar to those in standards within an order of magnitude. Therefore, analytical errors are estimated to be ~10%. The results are presented in Table 5.

## Results

*Mineral compositions*

*Olivine.* Mineral compositions in the composite xenolith vary dramatically between different zones (Tables 1–4). Olivine in the lherzolite broadly has a homogenous composition with low Fo (85–86), NiO (0.30–0.43 wt%), MnO (≤0.20 wt%), and CaO (<0.14 wt%), independent of the grain size. Olivine in the sheared mantle has a slightly lower Fo value (84–85.6) relative to olivine in the lherzolite and variable NiO (0.17–0.35 wt%), with low and variable MnO and CaO (Table 1). Olivine in the reactant rim is even lower in Fo (83–85) and NiO (0.11–0.31 wt%) than that in the sheared mantle, but has much higher MnO and CaO (Table 1). Clear zoning exists

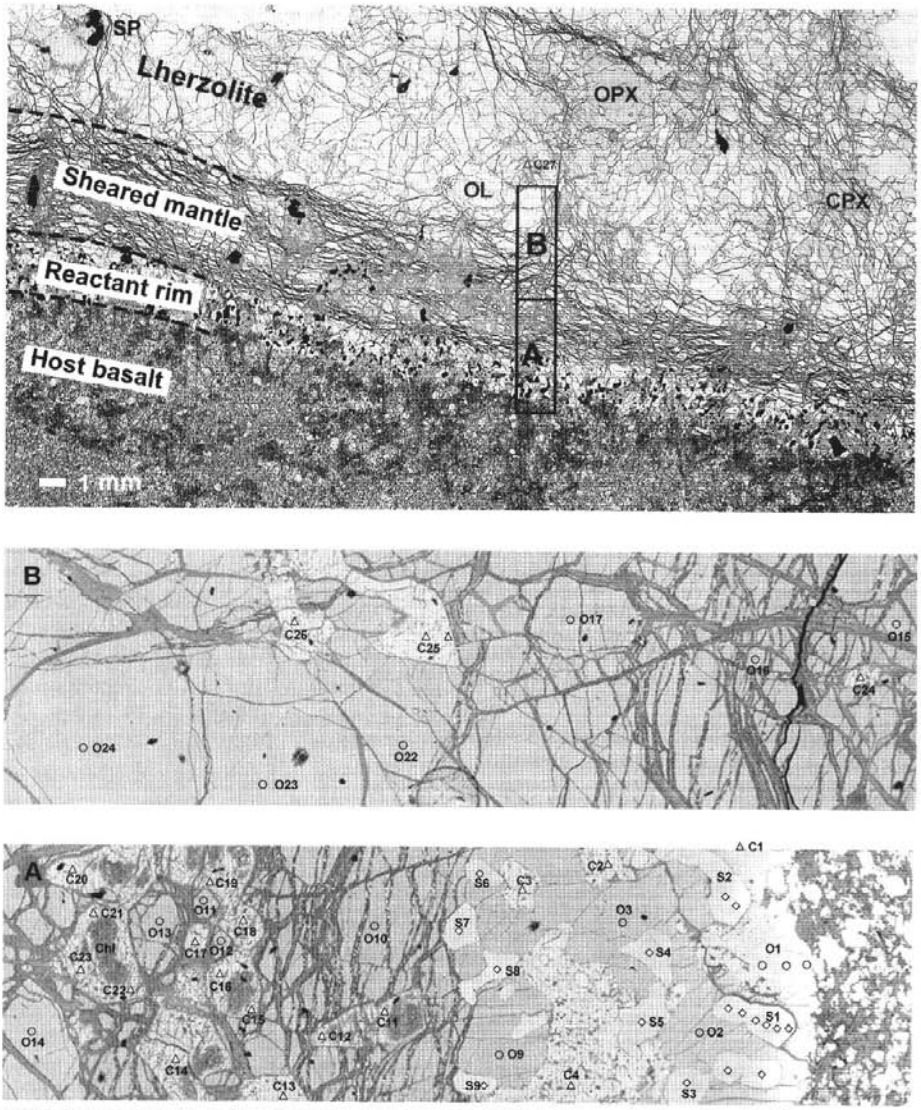



FIG. 2. Photograph of the composite xenolith (scale bar = 1 mm). A and B. Backscattered electron images for the traverse marked with the rectangle. Mineral abbreviations: OL = olivine; OPX = orthopyroxene; CPX = clinopyroxene; SP = spinel.

when olivine is in contact with the host basalt, so as to have extremely low Fo (down to 69.5) and high CaO and MnO (up to 0.55 wt% and 0.48 wt%, respectively) in the rim, approaching the composition of the olivine phenocryst (Figs. 2 and 4A). Thus the olivine in this composite xenolith displays a slight decrease in Fo and NiO and an increase in CaO and MnO from the lherzolite to the reactant rim. The low Fo value also makes this composite xenolith distinct from the peridotitic xenoliths (88–92) entrained in Cenozoic basalts on the craton (Fig. 4A). Olivine phenocrysts are low in Fo (≤72) and NiO and high in CaO and MnO (Table 1 and Fig. 4A).

This composite xenolith has olivine with extremely low Fo, the lowest Fo value observed

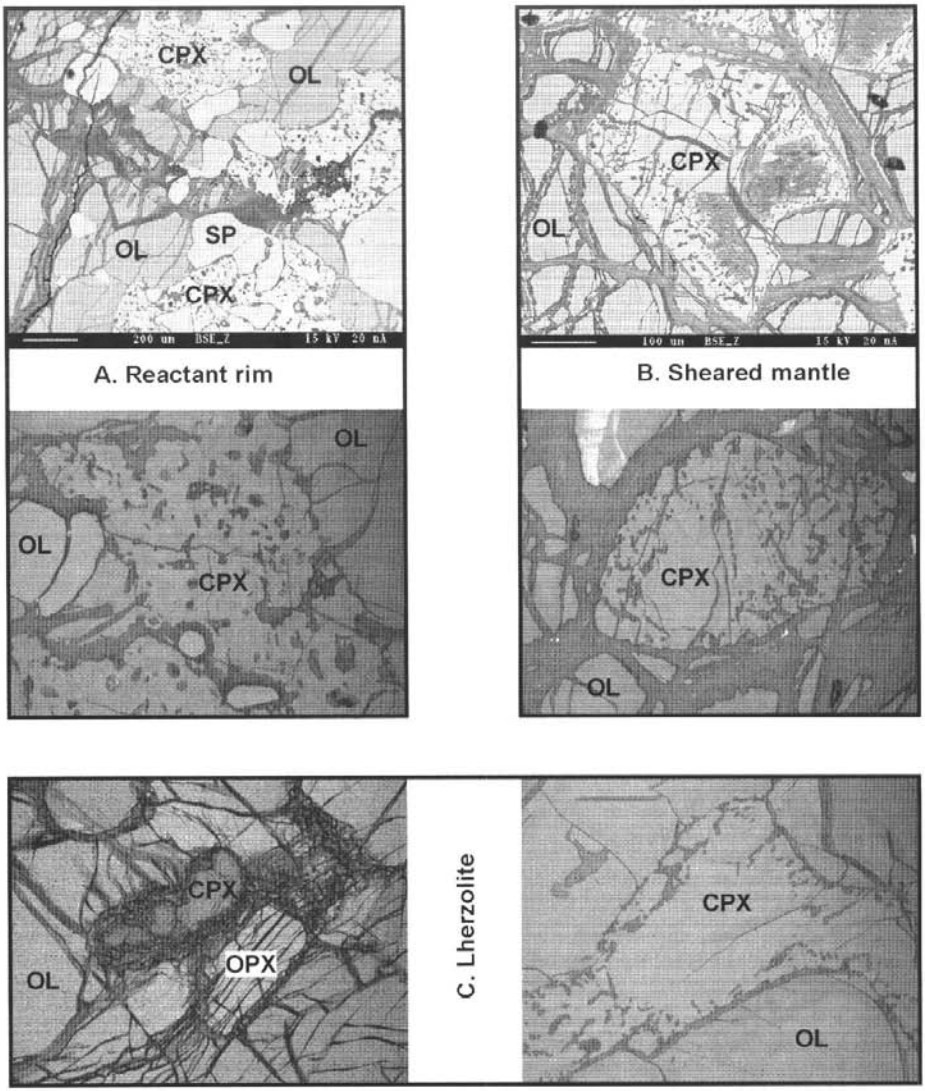



FIG. 3. Clinopyroxene texture in different zones of the xenolith. A. Backscattered image (upper) of mineral assemblage and reflected light (lower) of clinopyroxene in reactant rim. B. Backscattered image (upper) of mineral assemblage and reflected light (lower) of clinopyroxene in sheared mantle. C. Transmitted light (left) and reflected light (right) of clinopyroxene in the lherzolite. Width of field for A and B is 0.25 mm and for C is 1 mm.

globally in both kimberlite- and basalt-borne mantle peridotites (Dawson, 1980; Nixon, 1987; Boyd, 1989; Menzies, 1990; Boyd et al., 1997; Gaul et al., 2000; Walter, 2003). Such a feature also makes this xenolith completely distinct from garnet peridotites (Fo = 92–95) entrained in Paleozoic diamondiferous kimberlites of the North China craton (Chi and Lu, 1996; Fan et al., 2000; Zheng et al., 2001). Moreover, olivines from all the lherzolitic xenoliths in this area are low in Fo (Yan et al., 2003) (Fig. 4A). The very low Fo olivines also exist in spinel-facies lherzolitic xenoliths from the Cenozoic Shanwang basalt (Figs. 1 and 4B). Olivines for the peridotitic xenoliths from the Shanwang have Fo values dominantly in a range of 86~90 with some green ones as low as 83 (Wang et al., 1987; Zheng et al., 1998).

TABLE 1. Olivine Compositions in the Composite Xenolith and Host Basalt (wt%)[1]

| Olivine | $SiO_2$ | MgO | NiO | FeO | MnO | CaO | Total | Fo |
|---|---|---|---|---|---|---|---|---|
| | | | | Reactant rim | | | | |
| OL1-r | 37.82 | 36.16 | 0.17 | 25.37 | 0.50 | 0.39 | 100.4 | 71.8 |
| OL1-m | 38.56 | 39.33 | 0.20 | 22.06 | 0.36 | 0.19 | 100.7 | 76.1 |
| OL1-c | 37.44 | 40.14 | 0.15 | 20.56 | 0.32 | 0.33 | 98.9 | 77.7 |
| OL2 | 39.62 | 44.31 | 0.27 | 15.06 | 0.24 | 0.22 | 99.7 | 84.0 |
| OL3 | 39.29 | 44.64 | 0.26 | 14.13 | 0.16 | 0.22 | 98.7 | 84.9 |
| OL4-r | 36.76 | 34.70 | 0.11 | 27.15 | 0.51 | 0.45 | 99.7 | 69.5 |
| OL4-m | 36.83 | 35.09 | 0.14 | 26.81 | 0.55 | 0.48 | 99.9 | 70.0 |
| OL4-c | 39.23 | 45.13 | 0.25 | 14.44 | 0.24 | 0.18 | 99.5 | 84.8 |
| OL5-r | 36.73 | 34.57 | 0.12 | 27.38 | 0.55 | 0.40 | 99.7 | 69.2 |
| OL5-m1 | 37.32 | 37.78 | 0.19 | 23.34 | 0.46 | 0.42 | 99.5 | 74.3 |
| OL5-m2 | 39.19 | 41.73 | 0.19 | 17.80 | 0.23 | 0.29 | 99.4 | 80.7 |
| OL5-m3 | 39.48 | 44.12 | 0.27 | 15.83 | 0.20 | 0.21 | 100.1 | 83.2 |
| OL5-c | 39.61 | 45.05 | 0.19 | 14.43 | 0.18 | 0.08 | 99.5 | 84.8 |
| OL6 | 39.35 | 44.89 | 0.28 | 14.74 | 0.23 | 0.22 | 99.7 | 84.4 |
| OL7 | 38.73 | 45.11 | 0.27 | 14.26 | 0.21 | 0.13 | 98.7 | 84.9 |
| OL8 | 39.55 | 45.38 | 0.31 | 14.30 | 0.23 | 0.16 | 99.9 | 85.0 |
| OL9 | 39.60 | 44.96 | 0.30 | 14.46 | 0.19 | 0.26 | 99.8 | 84.7 |
| | | | | Sheared zone | | | | |
| OL10 | 39.19 | 45.52 | 0.35 | 14.27 | 0.17 | 0.14 | 99.6 | 85.0 |
| OL11 | 39.99 | 45.19 | 0.34 | 13.68 | 0.16 | 0.20 | 99.5 | 85.5 |
| OL12 | 39.45 | 45.43 | 0.31 | 14.22 | 0.23 | 0.26 | 99.9 | 85.1 |
| OL13-c | 40.03 | 45.52 | 0.32 | 13.62 | 0.12 | 0.16 | 99.8 | 85.6 |
| OL13-r | 39.61 | 45.07 | 0.19 | 14.49 | 0.21 | 0.24 | 99.8 | 84.7 |
| OL14 | 39.82 | 45.23 | 0.28 | 14.10 | 0.15 | 0.18 | 99.8 | 85.1 |
| OL15 | 39.54 | 45.70 | 0.32 | 13.97 | 0.17 | 0.08 | 99.8 | 85.4 |
| OL16 | 39.65 | 45.56 | 0.31 | 13.62 | 0.15 | 0.16 | 99.4 | 85.6 |
| OL17 | 39.56 | 45.43 | 0.17 | 13.95 | 0.17 | 0.09 | 99.4 | 85.3 |
| OL18 | 39.22 | 44.69 | 0.32 | 15.17 | 0.16 | 0.14 | 99.7 | 84.0 |
| OL19 | 39.87 | 44.86 | 0.25 | 14.80 | 0.14 | 0.07 | 100.0 | 84.4 |
| OL20 | 39.55 | 45.12 | 0.28 | 14.95 | 0.16 | 0.00 | 100.1 | 84.3 |
| OL21 | 39.64 | 45.50 | 0.34 | 14.47 | 0.15 | 0.06 | 100.2 | 84.9 |
| | | | | Lherzolite | | | | |
| OL22 | 40.18 | 45.76 | 0.30 | 13.76 | 0.10 | 0.09 | 100.2 | 85.6 |
| OL23 | 39.53 | 45.65 | 0.33 | 13.69 | 0.16 | 0.09 | 99.4 | 85.6 |
| OL24 | 39.63 | 45.63 | 0.34 | 14.03 | 0.12 | 0.09 | 99.8 | 85.3 |
| OL25 | 39.49 | 45.73 | 0.31 | 13.52 | 0.20 | 0.14 | 99.4 | 85.8 |
| OL26 | 40.08 | 45.91 | 0.39 | 13.06 | 0.19 | 0.09 | 99.7 | 86.2 |
| OL27 | 39.63 | 45.95 | 0.43 | 13.03 | 0.15 | 0.13 | 99.3 | 86.3 |
| OL28 | 39.88 | 45.89 | 0.31 | 13.29 | 0.20 | 0.09 | 99.7 | 86.0 |
| OL29 | 40.10 | 45.10 | 0.32 | 14.16 | 0.16 | 0.09 | 99.9 | 85.0 |
| | | | | Phenocryst | | | | |
| Grain 1 | 36.97 | 34.32 | 0.17 | 27.80 | 0.56 | 0.40 | 100.2 | 68.8 |
| Grain 2-c | 37.08 | 35.36 | 0.08 | 26.25 | 0.48 | 0.52 | 99.8 | 70.6 |
| Grain 2-r | 37.09 | 34.01 | 0.15 | 27.39 | 0.64 | 0.48 | 99.7 | 68.9 |
| Grain 3 | 37.78 | 36.38 | 0.11 | 25.18 | 0.54 | 0.43 | 100.4 | 72.0 |
| Grain 4 | 36.88 | 35.72 | 0.15 | 25.96 | 0.43 | 0.41 | 99.6 | 71.0 |

[1]C = core; m = mantle; r = rim.

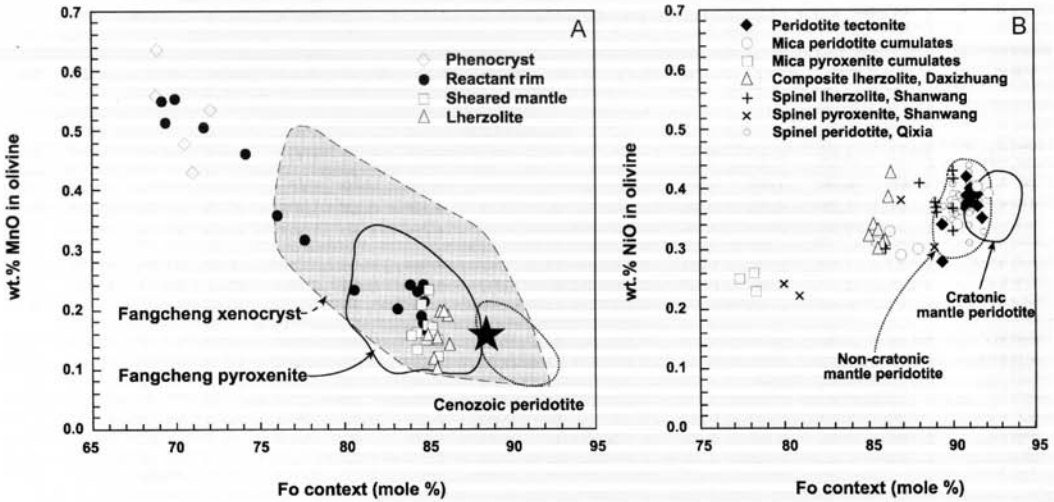



FIG. 4. Fo (mole%) vs. MnO wt% (A) and NiO wt% (B) in olivines. A. Cenozoic peridotite represents olivine from Cenozoic basalt-borne peridotitic xenoliths (Fan et al., 2000; Zheng et al., 2001). Fangcheng xenocryst and pyroxenite represents Fangcheng basalt-borne xenocrystic olivine or olivine from pyroxenite xenoliths (Zhang, 2005). The star represents the average composition of olivines from the spinel lherzolites in Daxizhuang (Yan et al., 2003). B. Fields of cratonic and non-cratonic mantle peridotites worldwide and data of peridotite tectonites and mica peridotite and pyroxenite cumulates are from Walter (2003). Data of spinel lherzolites and pyroxenites from Shanwang and Qixia are taken from Zheng et al. (1998) and Rudnick et al. (2004). Daxizhuang composite lherzolite is from this study.

Green olivines occur as fine grains interstitial to other minerals, and are interpreted as a result of mantle metasomatism (Wang et al., 1987). The NiO contents of olivines in this lherzolite are similar to those of olivines in spinel peridotitic xenoliths from Shanwang and Qixia and non-cratonic mantle peridotites worldwide (Fig. 4B) although the latter have higher Fo (Wang et al., 1987; Zheng et al., 1998; Walter, 2003; Rudnick et al., 2004).

*Clinopyroxene*. Clinopyroxene also displays a clear compositional trend from the lherzolite to the reactant rim, with a decrease in enstatite component and $Cr_2O_3$ and $Na_2O$ contents and an increase in CaO and $TiO_2$ (Table 2 and Fig. 5). The clinopyroxenes in the lherzolite are augite according to Wo-En-Fs nomenclature (Fig. 5). They have slightly higher Mg# (84.6–87.7) and $Cr_2O_3$ (0.91–1.58 wt%) and lower $TiO_2$ (0.42–0.98 wt%) than their counterparts in the sheared mantle (Mg# = 84.1–87.3; $Cr_2O_3$ = 0.45–0.75 wt%; $TiO_2$ = 1.0–1.7 wt%), with an exception for grain 25, which is adjacent to the sheared mantle and has a compositional zoning (Table 2). As for the $Na_2O$ contents, two groups of clinopyroxenes exist in the lherzolite: the dominant high $Na_2O$ (1.2–1.6 wt%) clinopyroxenes occur as coarser grains with relatively higher Mg# and lower $Al_2O_3$ (Table 2). In contrast, the low $Na_2O$ (~0.5 wt%) clinopyroxenes occur as fine grains with sieve-texture (Fig. 3C). The compositions for most clinopyroxenes in the lherzolite are similar to that for clinopyroxenes from pyroxenite xenoliths in Cenozoic basalts rather than diopsides from peridotitic xenoliths in Paleozoic kimberlites or Cenozoic basalts (Fig. 6A). Few low-$Na_2O$ clinopyroxenes fall within the field of augites from pyroxenite xenoliths entrained in Mesozoic basalts (Fig. 6A). However, high $Al_2O_3$ contents, similar to the clinopyroxenes from Shanwang and Qixia and non-cratonic peridotitic xenoliths worldwide (Zheng et al., 1998; Rudnick et al., 2004), make this lherzolite distinct from mica peridotitic and pyroxenitic cumulates (Fig. 6B) (Walter, 2003).

The sheared mantle also contains two groups of clinopyroxenes (Table 2). High-$Na_2O$ clinopyroxenes form the clean cores and low $Na_2O$ ones in the rims (Figs. 3 and 5). High-$Na_2O$ clinopyroxene is characterized by low Mg# and Wo and high $Al_2O_3$ and plots within the field of pyroxenite xenoliths from Cenozoic basalts (Fig. 6a), and thus is augite (Fig. 5). In contrast, the low-$Na_2O$ clinopyroxene is

TABLE 2. Clinopyroxene (CPX) Compositions in the Composite Xenolith (wt%)[1]

| CPX | $SiO_2$ | $TiO_2$ | $Al_2O_3$ | $Cr_2O_3$ | MgO | CaO | MnO | FeO | $Na_2O$ | Total | Mg# | WO | EN | FS |
|---|---|---|---|---|---|---|---|---|---|---|---|---|---|---|
| | | | | | | Reactant rim | | | | | | | | |
| CPX1-c | 49.15 | 1.88 | 6.67 | 0.35 | 14.10 | 22.13 | 0.13 | 5.18 | 0.54 | 100.1 | 82.9 | 48.22 | 42.74 | 9.04 |
| CPX1-r | 46.84 | 2.80 | 7.84 | 0.25 | 12.50 | 22.27 | 0.09 | 6.59 | 0.56 | 99.7 | 77.2 | 49.62 | 38.75 | 11.63 |
| CPX2* | 51.70 | 1.20 | 4.48 | 0.34 | 15.86 | 21.96 | 0.11 | 4.13 | 0.45 | 100.2 | 87.3 | 46.39 | 46.62 | 6.99 |
| CPX3 | 50.62 | 1.42 | 8.17 | 0.43 | 14.49 | 18.67 | 0.10 | 4.83 | 1.49 | 100.2 | 84.3 | 43.74 | 47.24 | 9.02 |
| CPX4-r | 50.29 | 1.44 | 5.56 | 0.33 | 14.81 | 21.99 | 0.09 | 4.48 | 0.53 | 99.5 | 85.6 | 47.64 | 44.64 | 7.72 |
| CPX4-c | 49.35 | 1.73 | 7.26 | 0.50 | 14.36 | 22.20 | 0.07 | 4.25 | 0.55 | 100.3 | 85.7 | 48.73 | 43.86 | 7.41 |
| CPX5* | 49.17 | 2.02 | 6.30 | 0.31 | 13.58 | 22.52 | 0.15 | 5.36 | 0.57 | 100.0 | 81.9 | 49.26 | 41.33 | 9.41 |
| CPX6* | 48.52 | 2.32 | 6.53 | 0.33 | 13.41 | 22.45 | 0.13 | 5.67 | 0.48 | 99.8 | 80.9 | 49.19 | 40.89 | 9.92 |
| CPX7* | 49.20 | 2.35 | 5.23 | 0.34 | 13.81 | 22.71 | 0.12 | 5.47 | 0.51 | 99.8 | 81.9 | 49.06 | 41.51 | 9.43 |
| CPX8* | 50.64 | 1.94 | 4.77 | 0.24 | 14.80 | 22.74 | 0.05 | 4.27 | 0.46 | 99.9 | 86.1 | 48.69 | 44.09 | 7.22 |
| CPX9-c | 50.26 | 1.84 | 5.39 | 0.45 | 14.50 | 22.45 | 0.03 | 4.32 | 0.52 | 99.7 | 85.8 | 48.78 | 43.84 | 7.38 |
| CPX9-r | 48.93 | 2.56 | 4.91 | 0.04 | 12.52 | 22.00 | 0.13 | 7.42 | 0.87 | 99.4 | 75.1 | 48.55 | 38.45 | 13.00 |
| CPX10* | 50.97 | 1.32 | 5.19 | 0.57 | 15.14 | 21.98 | 0.13 | 4.21 | 0.59 | 100.1 | 86.5 | 47.33 | 45.36 | 7.30 |
| | | | | | | Sheared zone | | | | | | | | |
| CPX11 | 50.99 | 1.38 | 8.08 | 0.50 | 14.72 | 18.61 | 0.15 | 4.98 | 1.43 | 100.8 | 84.1 | 43.18 | 47.52 | 9.30 |
| CPX12 | 50.85 | 1.25 | 7.82 | 0.45 | 14.97 | 18.69 | 0.04 | 4.76 | 1.37 | 100.2 | 84.9 | 43.20 | 48.14 | 8.66 |
| CPX13 | 50.70 | 1.27 | 7.90 | 0.47 | 14.69 | 18.80 | 0.12 | 4.74 | 1.48 | 100.2 | 84.6 | 43.69 | 47.50 | 8.82 |
| CPX14-c | 51.06 | 1.20 | 7.99 | 0.63 | 14.81 | 18.70 | 0.06 | 4.60 | 1.55 | 100.6 | 85.1 | 43.54 | 47.98 | 8.48 |
| CPX14-r | 49.98 | 1.63 | 6.47 | 0.61 | 14.75 | 21.32 | 0.11 | 4.36 | 0.58 | 99.8 | 85.9 | 47.03 | 45.27 | 7.71 |
| CPX15 | 50.51 | 1.00 | 7.60 | 0.53 | 14.91 | 19.12 | 0.11 | 4.90 | 1.26 | 99.9 | 84.4 | 43.68 | 47.39 | 8.93 |
| CPX16 | 50.27 | 1.27 | 7.74 | 0.55 | 14.71 | 18.78 | 0.14 | 4.66 | 1.44 | 99.5 | 84.9 | 43.68 | 47.61 | 8.71 |
| CPX17* | 50.26 | 1.80 | 5.72 | 0.69 | 14.83 | 21.99 | 0.14 | 4.25 | 0.59 | 100.3 | 86.1 | 47.75 | 44.81 | 7.45 |
| CPX18 | 50.72 | 1.20 | 7.87 | 0.46 | 14.81 | 18.60 | 0.15 | 4.92 | 1.38 | 100.1 | 84.3 | 43.09 | 47.74 | 9.17 |
| CPX19* | 52.32 | 0.93 | 3.67 | 0.53 | 16.16 | 21.55 | 0.13 | 4.19 | 0.52 | 100.0 | 87.3 | 45.45 | 47.43 | 7.12 |
| CPX20* | 50.69 | 1.41 | 5.82 | 0.61 | 15.11 | 21.50 | 0.14 | 4.53 | 0.60 | 100.4 | 85.6 | 46.57 | 45.54 | 7.89 |
| CPX21 | 50.68 | 1.22 | 7.58 | 0.53 | 14.88 | 18.47 | 0.09 | 4.83 | 1.49 | 99.8 | 84.6 | 42.94 | 48.13 | 8.94 |
| CPX22* | 50.39 | 1.70 | 5.62 | 0.71 | 14.86 | 22.03 | 0.08 | 4.44 | 0.59 | 100.4 | 85.6 | 47.65 | 44.72 | 7.63 |
| CPX23* | 51.49 | 1.52 | 4.00 | 0.60 | 15.38 | 22.17 | 0.09 | 4.20 | 0.50 | 99.9 | 86.7 | 47.25 | 45.61 | 7.14 |
| CPX24* | 52.53 | 1.29 | 3.51 | 0.75 | 16.74 | 20.64 | 0.10 | 4.35 | 0.54 | 100.5 | 87.3 | 43.54 | 49.13 | 7.33 |
| | | | | | | Lherzolite | | | | | | | | |
| CPX25-r | 51.24 | 1.09 | 4.93 | 0.94 | 15.88 | 20.94 | 0.07 | 4.40 | 0.55 | 100.0 | 86.6 | 45.01 | 47.49 | 7.50 |
| CPX25-c | 51.83 | 1.01 | 6.85 | 0.80 | 15.06 | 18.59 | 0.10 | 4.60 | 1.46 | 100.3 | 85.4 | 43.02 | 48.49 | 8.49 |
| CPX26 | 51.51 | 0.98 | 6.85 | 0.96 | 15.55 | 18.56 | 0.13 | 4.79 | 1.22 | 100.6 | 85.2 | 42.15 | 49.13 | 8.72 |
| CPX27 | 51.57 | 0.89 | 6.42 | 0.91 | 15.28 | 18.63 | 0.15 | 4.40 | 1.56 | 99.8 | 86.1 | 42.89 | 48.94 | 8.17 |
| CPX28 | 52.04 | 0.76 | 5.70 | 1.43 | 15.59 | 18.67 | 0.11 | 4.22 | 1.41 | 99.9 | 86.8 | 42.68 | 49.59 | 7.73 |
| CPX29 | 52.96 | 0.47 | 4.23 | 1.29 | 16.35 | 18.61 | 0.06 | 4.36 | 1.49 | 99.8 | 87.0 | 41.53 | 50.77 | 7.70 |
| CPX30 | 53.33 | 0.46 | 4.71 | 1.58 | 16.05 | 18.86 | 0.06 | 4.22 | 1.44 | 100.7 | 87.2 | 42.35 | 50.15 | 7.51 |
| CPX31 | 51.97 | 0.69 | 5.73 | 1.15 | 15.49 | 18.58 | 0.13 | 4.32 | 1.42 | 99.5 | 86.4 | 42.61 | 49.43 | 7.97 |
| CPX32* | 51.11 | 0.77 | 4.25 | 1.19 | 16.23 | 21.24 | 0.16 | 4.26 | 0.49 | 99.7 | 87.1 | 44.93 | 47.77 | 7.30 |
| CPX33 | 51.38 | 0.73 | 6.01 | 1.19 | 15.49 | 18.44 | 0.15 | 4.97 | 1.48 | 99.9 | 84.8 | 41.92 | 48.99 | 9.09 |
| CPX34 | 51.98 | 0.77 | 5.75 | 1.32 | 15.57 | 18.56 | 0.06 | 4.86 | 1.52 | 100.4 | 85.1 | 42.12 | 49.16 | 8.72 |
| CPX35 | 50.12 | 0.92 | 6.84 | 1.08 | 15.36 | 18.47 | 0.09 | 4.95 | 1.46 | 99.3 | 84.6 | 42.19 | 48.82 | 8.99 |
| CPX36 | 51.66 | 0.88 | 6.61 | 0.94 | 15.24 | 18.44 | 0.11 | 4.90 | 1.58 | 100.3 | 84.7 | 42.34 | 48.68 | 8.98 |
| CPX37 | 51.08 | 0.69 | 5.52 | 1.31 | 15.89 | 18.34 | 0.24 | 4.73 | 1.50 | 99.3 | 85.7 | 41.37 | 49.87 | 8.76 |
| CPX38* | 51.95 | 0.64 | 3.30 | 1.37 | 16.82 | 20.57 | 0.11 | 4.22 | 0.49 | 99.5 | 87.7 | 43.44 | 49.42 | 7.15 |
| CPX39 | 51.73 | 0.43 | 4.38 | 1.50 | 16.38 | 18.63 | 0.24 | 4.71 | 1.42 | 99.4 | 86.1 | 41.14 | 50.32 | 8.54 |
| CPX40 | 53.19 | 0.42 | 4.41 | 1.42 | 16.23 | 18.44 | 0.08 | 4.73 | 1.46 | 100.4 | 86.0 | 41.18 | 50.43 | 8.39 |
| CPX41 | 52.33 | 0.42 | 4.40 | 1.43 | 16.31 | 18.37 | 0.13 | 4.75 | 1.40 | 99.5 | 85.9 | 40.94 | 50.57 | 8.49 |

[1]C = core; r = rim; Mg# = 100Mg/(Mg + Fe) atomic ratio; * = clinopyroxene with sieve texture rather than the clean portion; Cpx 30 is the largest grain.

TABLE 3. Orthopyroxene Compositions in the Lherzolite of the Composite Xenolith (wt%)

| | $SiO_2$ | $TiO_2$ | $Al_2O_3$ | $Cr_2O_3$ | MgO | CaO | MnO | FeO | $Na_2O$ | Total | Mg# | WO | EN | FS |
|---|---|---|---|---|---|---|---|---|---|---|---|---|---|---|
| Grain 1 | 55.04 | 0.29 | 4.39 | 0.53 | 30.59 | 1.07 | 0.19 | 8.42 | 0.15 | 100.7 | 86.6 | 2.13 | 84.52 | 13.35 |
| Grain 2 | 54.66 | 0.21 | 4.29 | 0.54 | 30.73 | 1.09 | 0.19 | 8.36 | 0.12 | 100.2 | 86.7 | 2.16 | 84.63 | 13.22 |
| Grain 3 | 55.34 | 0.20 | 4.11 | 0.56 | 30.82 | 1.08 | 0.15 | 8.27 | 0.14 | 100.7 | 86.9 | 2.14 | 84.86 | 13.01 |
| Grain 4 | 55.48 | 0.14 | 3.45 | 0.64 | 31.01 | 1.10 | 0.16 | 8.46 | 0.18 | 100.6 | 86.7 | 2.16 | 84.63 | 13.21 |
| Grain 5 | 55.45 | 0.25 | 3.78 | 0.57 | 30.83 | 1.08 | 0.21 | 8.42 | 0.16 | 100.8 | 86.7 | 2.13 | 84.59 | 13.28 |
| Grain 6 | 54.23 | 0.25 | 4.09 | 0.61 | 30.44 | 1.17 | 0.17 | 9.16 | 0.10 | 100.2 | 85.6 | 2.30 | 83.37 | 14.33 |
| Grain 7 | 53.78 | 0.24 | 3.92 | 0.57 | 30.39 | 1.12 | 0.19 | 9.27 | 0.17 | 99.6 | 85.4 | 2.21 | 83.26 | 14.54 |
| Grain 8 | 53.49 | 0.23 | 3.81 | 0.61 | 30.80 | 1.14 | 0.19 | 9.36 | 0.16 | 99.8 | 85.4 | 2.22 | 83.29 | 14.49 |
| Grain 9 | 53.94 | 0.24 | 3.96 | 0.63 | 30.46 | 1.13 | 0.18 | 9.32 | 0.09 | 99.9 | 85.4 | 2.22 | 83.21 | 14.57 |
| Grain 10 | 55.13 | 0.13 | 3.59 | 0.69 | 30.65 | 1.06 | 0.21 | 9.09 | 0.12 | 100.7 | 85.7 | 2.08 | 83.67 | 14.25 |
| Grain 11 | 54.79 | 0.15 | 3.12 | 0.62 | 31.07 | 1.14 | 0.17 | 8.71 | 0.15 | 99.9 | 86.4 | 2.22 | 84.27 | 13.51 |

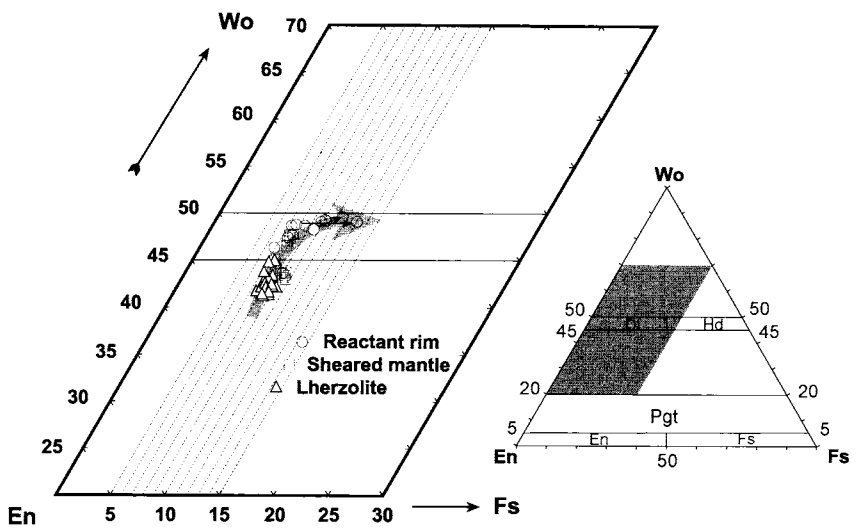



FIG. 5. Pyroxene nomenclature based on Wo-En-Fs end members. The arrow shows the compositional trend from the lherzolite to the reactant rim.

characterized by slightly higher Mg# and lower $Al_2O_3$ and falls within the field of pyroxenite xenoliths from Mesozoic basalts (Fig. 6A). These low-$Na_2O$ clinopyroxenes can be termed diopside (Fig. 5). The clinopyroxenes in the reactant rim are all titaniferous augites with very low enstatite (38.4–47.2). These clinopyroxenes have very low $Na_2O$ and $Cr_2O_3$ (<0.6 wt%) and high $TiO_2$ (1.2–2.8 wt%). Such a chemical feature is completely different from that of diopsides from peridotitic and pyroxenite xenoliths from either Paleozoic kimberlites or Cenozoic basalts, but is similar to that of xenocrystic clinopyroxenes and pyroxenite xenoliths from Mesozoic basalts (Fig. 6A). Clinopyroxenes in contact with the host basalt also show apparent zoning with lower Mg# and $Cr_2O_3$ and higher $TiO_2$ and Fs contents toward the rim (Table 2 and Figs. 5 and 6A).

*Orthopyroxene.* Orthopyroxene in the lherzolite has high $Cr_2O_3$, CaO (>1 wt%), and low Mg# (<87)

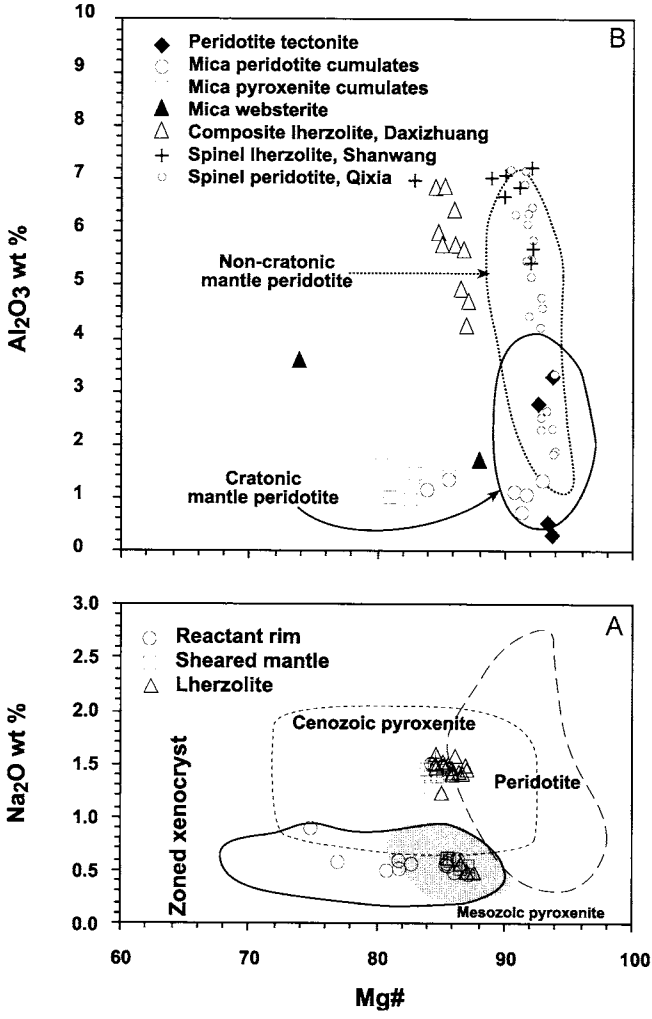



FIG. 6. Mg# vs. $Na_2O$ wt% (A) and $Al_2O_3$ wt% (B) in clinopyroxenes. A. Fields for Cenozoic and Paleozoic peridotitic xenoliths, Cenozoic pyroxenites, Mesozoic pyroxenites, and xenocryst from Fangcheng basalts are from the published literature. B. Fields of cratonic and non-cratonic mantle peridotites worldwide and data of peridotite tectonites, mica peridotite and pyroxenite cumulates and mica websterite are from Water (2003). Data of spinel lherzolites from the Shanwang and Qixia are taken from Zheng et al. (1998) and Rudnick et al. (2004). Composite lherzolite is from this study.

and enstatite contents (83.2–84.9). The low Mg# is distinctive from that of residue peridotites worldwide, but is similar to the orthopyroxene from reactive harzburgite xenoliths (Zhang et al., 2001a; Xu et al., 2003).

*Spinel.* Spinel in this composite xenolith displays a clear compositional trend, with a dramatic drop in $Cr_2O_3$ and an increase in $Al_2O_3$, resulting in a decrease in Cr# from the lherzolite (25.5–38.0) through the sheared mantle (7.9–14.8) to the reactant rim (3.2–4.7) (Table 4 and Fig. 7). Two trends are observed (Fig. 7): one is from the lherzolite to the reactant rim, as shown by the decrease in Cr# and increase in Mg#, and the other is within the reactant rim and characterized by continuous decrease in Mg# with relatively constant Cr#. The latter trend was produced by interaction with the host magma. Such a compositional feature of spinel in the composite

TABLE 4. Spinel Compositions in the Composite Xenolith (wt%)[1]

| SP | $TiO_2$ | $Al_2O_3$ | $Cr_2O_3$ | $Fe_2O_3$ | MgO | MnO | FeO | NiO | Total | Cr# | Mg# |
|---|---|---|---|---|---|---|---|---|---|---|---|
| | | | | | Reactant rim | | | | | | |
| SP1-1r | 0.84 | 54.10 | 3.07 | 10.59 | 15.54 | 0.20 | 16.41 | 0.28 | 101.0 | 3.66 | 62.8 |
| SP1-2 | 0.50 | 57.66 | 3.26 | 7.64 | 17.95 | 0.19 | 13.21 | 0.36 | 100.8 | 3.65 | 70.8 |
| SP1-3 | 0.50 | 57.96 | 3.26 | 7.46 | 18.76 | 0.16 | 11.90 | 0.43 | 100.4 | 3.63 | 73.8 |
| SP1-4 | 0.59 | 57.89 | 3.34 | 6.99 | 18.74 | 0.16 | 11.76 | 0.42 | 99.9 | 3.72 | 74.0 |
| SP1-5 | 0.58 | 58.04 | 3.55 | 6.87 | 18.96 | 0.14 | 11.60 | 0.35 | 100.1 | 3.94 | 74.4 |
| SP1-6c | 0.58 | 58.04 | 3.55 | 6.87 | 18.96 | 0.14 | 11.60 | 0.35 | 100.1 | 3.94 | 74.4 |
| SP2-r | 0.79 | 56.38 | 2.73 | 8.58 | 17.11 | 0.19 | 14.04 | 0.31 | 100.1 | 3.15 | 68.5 |
| SP2-c | 0.57 | 54.70 | 2.96 | 9.55 | 15.83 | 0.22 | 15.57 | 0.36 | 99.8 | 3.50 | 64.4 |
| SP3-r | 0.64 | 55.93 | 3.13 | 8.57 | 16.71 | 0.17 | 14.65 | 0.24 | 100.0 | 3.61 | 67.0 |
| SP3-m | 0.49 | 57.24 | 3.25 | 7.87 | 17.39 | 0.12 | 14.09 | 0.37 | 100.8 | 3.67 | 68.7 |
| SP3-c | 0.50 | 60.37 | 3.73 | 4.50 | 19.32 | 0.06 | 11.39 | 0.37 | 100.2 | 3.98 | 75.1 |
| SP4 | 0.55 | 59.17 | 4.07 | 5.14 | 18.91 | 0.15 | 11.92 | 0.38 | 100.3 | 4.41 | 73.9 |
| SP5 | 0.55 | 58.02 | 4.17 | 5.63 | 19.12 | 0.12 | 10.82 | 0.38 | 98.8 | 4.60 | 75.9 |
| SP6 | 0.53 | 58.19 | 5.01 | 4.76 | 18.75 | 0.09 | 11.92 | 0.26 | 99.5 | 5.46 | 73.7 |
| SP7 | 0.51 | 58.50 | 5.16 | 4.66 | 19.08 | 0.17 | 11.47 | 0.32 | 99.9 | 5.59 | 74.8 |
| SP8 | 0.50 | 59.27 | 5.05 | 3.99 | 18.85 | 0.10 | 11.94 | 0.39 | 100.1 | 5.40 | 73.8 |
| SP9 | 0.57 | 59.95 | 3.98 | 4.34 | 18.78 | 0.11 | 12.23 | 0.43 | 100.4 | 4.27 | 73.2 |
| SP10 | 0.56 | 58.95 | 4.30 | 5.19 | 18.85 | 0.16 | 12.08 | 0.27 | 100.4 | 4.66 | 73.6 |
| | | | | | Sheared zone | | | | | | |
| SP11 | 0.55 | 56.57 | 7.97 | 3.96 | 18.65 | 0.10 | 11.85 | 0.34 | 100.0 | 8.63 | 73.7 |
| SP12 | 0.52 | 56.09 | 8.01 | 4.56 | 18.90 | 0.11 | 11.48 | 0.27 | 99.9 | 8.74 | 74.6 |
| SP13 | 0.52 | 55.95 | 7.19 | 5.16 | 18.79 | 0.19 | 11.16 | 0.38 | 99.3 | 7.93 | 75.0 |
| SP14 | 0.56 | 54.95 | 8.59 | 4.70 | 18.65 | 0.12 | 11.40 | 0.36 | 99.3 | 9.49 | 74.5 |
| SP15 | 0.69 | 50.52 | 13.10 | 5.41 | 17.97 | 0.09 | 11.99 | 0.32 | 100.1 | 14.81 | 72.8 |
| SP16 | 0.55 | 53.86 | 10.25 | 4.63 | 18.09 | 0.18 | 12.21 | 0.35 | 100.1 | 11.32 | 72.5 |
| | | | | | Lherzolite | | | | | | |
| SP17 | 0.84 | 40.15 | 23.76 | 5.57 | 15.62 | 0.17 | 14.03 | 0.24 | 100.4 | 28.41 | 66.5 |
| SP18 | 0.77 | 42.69 | 21.72 | 5.10 | 16.04 | 0.12 | 13.85 | 0.28 | 100.6 | 25.45 | 67.4 |
| SP19 | 0.88 | 41.46 | 23.03 | 5.13 | 15.88 | 0.15 | 14.03 | 0.29 | 100.9 | 27.15 | 66.9 |
| SP20 | 0.99 | 38.61 | 22.89 | 7.27 | 14.74 | 0.25 | 14.94 | 0.18 | 99.9 | 28.46 | 63.8 |
| SP21 | 1.02 | 37.78 | 24.39 | 7.06 | 14.76 | 0.13 | 15.10 | 0.21 | 100.5 | 30.21 | 63.5 |
| SP22 | 1.08 | 32.04 | 29.37 | 7.98 | 13.75 | 0.17 | 15.63 | 0.18 | 100.2 | 38.08 | 61.1 |
| SP23 | 1.04 | 33.51 | 28.38 | 7.76 | 14.22 | 0.22 | 15.19 | 0.16 | 100.5 | 36.24 | 62.5 |

[1]C = core; m = mantle; r = rim; Cr# = 100Cr/(Cr+Al) atomic ratio and Mg# = 100Mg/(Mg+$Fe^{2+}$) atomic ratio.

xenolith is different from that of chromites from peridotitic xenoliths in Paleozoic kimberlites or Cenozoic basalts on the craton (Fig. 7), but is similar to that of spinel from peridotitic xenoliths in the Shanwang basalt. The Cr# and Mg# contents generally fall within the low Mg# part of the field for non-cratonic mantle peridotites (Fig. 7; Walter, 2003). Low Cr# in spinels makes this composite xenolith distinct from high Cr# and very low Mg# spinels observed in peridotitic and pyroxenitic cumulates (Fig. 7).

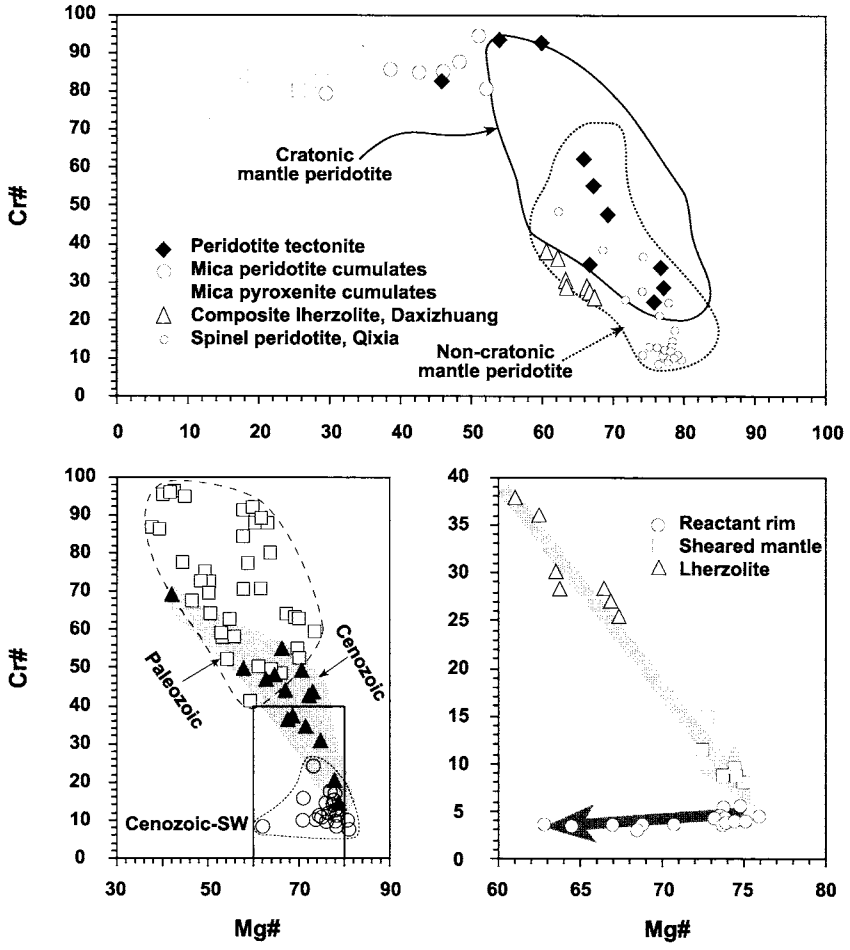



FIG. 7. Mg# (100Mg/(Mg + Fe)) vs. Cr# (100Cr/(Cr + Al)) in spinels. Data for spinels from peridotitic xenoliths in Paleozoic kimberlites and Cenozoic basalts are after Zheng et al. (2001). Fields of cratonic and non-cratonic mantle peridotites worldwide and data of peridotite tectonites and mica peridotite and pyroxenite cumulates are from Walter (2003). Figure at bottom right is the magnification of the rectangle in the figure at the bottom left. The shaded arrow shows the compositional trend.

*Trace element geochemistry*

Trace element concentrations of clinopyroxenes in the composite xenolith also show a clear variation in different zones (Table 5 and Fig. 8). In general, REE and other incompatible trace element (e.g., Y, Zr, Nb) concentrations systematically increase from the lherzolite to reactant rim, and all the clinopyroxenes have similar convex-upward chondrite-normalized REE patterns with Nd at the maximum (Table 5 and Fig. 8). Clinopyroxenes in the lherzolite have low REE (ΣREE = 42–64 ppm), Sr (133–141 ppm), Y (10.8–17.6 ppm), Zr (36–84 ppm) and Nb (<1.2 ppm) abundances (Table 5 and Fig. 8). Variations between different grains in the lherzolite are apparent in these clinopyroxenes with the lowest trace element concentration observed in a largest grain (Cpx30), although its rim has slightly higher REE, Y, and Zr (Table 5). Similarly, sieve-textured grains (Cpx32 and Cpx38) also have higher abundances in nearly all trace elements than clean grains (Table 5). One interesting feature is that clinopyroxenes in the lherzolite have slightly different REE patterns, with very low Lu (<0.1 ppm) abundances, distinguishable from clinopyroxenes in other zones

TABLE 5. Trace Element Concentrations (SIMS, ppm) of Clinopyroxenes (Cpx) in the Composite Xenolith[1]

| Cpx | La | Ce | Pr | Nd | Sm | Eu | Gd | Dy | Er | Yb | Lu | Hf | Sr | Y | Zr | Nb | ΣREE | Eu/Eu* | Zr/Zr* |
|---|---|---|---|---|---|---|---|---|---|---|---|---|---|---|---|---|---|---|---|
| Reactant rim | | | | | | | | | | | | | | | | | | | |
| Cpx1-1 | 9.52 | 32.1 | 5.76 | 33.3 | 9.55 | 2.96 | 9.55 | 6.84 | 2.46 | 1.66 | 0.203 | 5.89 | 151 | 30.6 | 186 | 2.38 | 114 | 0.93 | 0.68 |
| Cpx1-2 | 9.35 | 28.0 | 5.25 | 26.2 | 8.38 | 2.58 | 8.04 | 5.76 | 1.71 | 1.12 | 0.147 | 2.21 | 346 | 24.3 | 137 | 9.57 | 97 | 0.94 | 0.61 |
| Cpx1-3 | 7.67 | 25.0 | 4.36 | 27.8 | 8.50 | 2.67 | 8.77 | 5.73 | 1.89 | 1.57 | 0.210 | 2.89 | 122 | 26.3 | 130 | 7.08 | 94 | 0.93 | 0.55 |
| Cpx1-4 | 6.86 | 24.6 | 4.65 | 25.2 | 7.33 | 2.62 | 8.64 | 5.62 | 1.59 | 1.25 | 0.161 | 4.39 | 119 | 25.3 | 115 | 2.43 | 89 | 1.00 | 0.55 |
| Cpx1-5 | 8.12 | 27.0 | 4.79 | 28.5 | 8.58 | 2.92 | 9.02 | 5.84 | 1.81 | 1.46 | 0.176 | 3.91 | 114 | 27.3 | 125 | 2.00 | 98 | 1.00 | 0.52 |
| Cpx1-6 | 9.57 | 28.5 | 5.57 | 32.8 | 8.60 | 2.72 | 8.63 | 5.89 | 1.57 | 1.22 | 0.157 | 4.59 | 118 | 28.3 | 136 | 2.56 | 105 | 0.95 | 0.53 |
| Cpx2 | 8.75 | 27.5 | 5.29 | 31.1 | 9.75 | 2.92 | 8.56 | 5.47 | 1.94 | 1.44 | 0.177 | 5.51 | 124 | 27.5 | 131 | 1.99 | 103 | 0.95 | 0.49 |
| Cpx3 | 5.17 | 18.9 | 3.49 | 25.7 | 7.81 | 2.48 | 8.06 | 5.27 | 2.10 | 1.12 | 0.140 | 4.84 | 83.8 | 23.2 | 105 | 0.97 | 80 | 0.94 | 0.48 |
| Cpx4 | 4.79 | 15.1 | 3.19 | 20.2 | 6.23 | 2.08 | 6.70 | 5.68 | 1.95 | 1.25 | 0.135 | 3.61 | 59.2 | 21.0 | 87.8 | 0.78 | 67 | 0.97 | 0.51 |
| Cpx9-1 | 6.00 | 20.7 | 4.03 | 23.1 | 7.16 | 2.84 | 7.93 | 5.65 | 2.06 | 1.25 | 0.152 | 5.50 | 200 | 22.4 | 114 | 3.71 | 81 | 1.14 | 0.58 |
| Cpx9-2 | 7.89 | 23.9 | 4.60 | 27.3 | 8.15 | 3.11 | 8.12 | 6.66 | 2.72 | 1.49 | 0.177 | 4.45 | 125 | 26.9 | 124 | 3.62 | 94 | 1.15 | 0.54 |
| Cpx9-3 | 12.0 | 32.1 | 5.69 | 32.2 | 10.4 | 3.70 | 10.4 | 6.53 | 2.79 | 1.61 | 0.163 | 6.12 | 156 | 31.2 | 151 | 8.34 | 118 | 1.07 | 0.54 |
| Cpx10-1 | 10.9 | 31.1 | 4.99 | 28.9 | 8.70 | 3.10 | 8.91 | 4.74 | 1.91 | 1.29 | 0.159 | 3.46 | 148 | 26.1 | 109 | 6.04 | 105 | 1.06 | 0.45 |
| Cpx10-2 | 6.65 | 23.0 | 4.20 | 28.4 | 8.20 | 2.56 | 8.36 | 5.33 | 2.19 | 1.23 | 0.149 | 2.85 | 105 | 24.7 | 104 | 1.77 | 90 | 0.93 | 0.45 |
| Cpx10-3 | 5.07 | 18.5 | 3.42 | 25.2 | 7.66 | 2.43 | 7.49 | 5.17 | 2.06 | 1.10 | 0.137 | 4.74 | 82.2 | 22.8 | 103 | 0.95 | 78 | 0.96 | 0.49 |
| Sheared zone | | | | | | | | | | | | | | | | | | | |
| Cpx13 | 5.28 | 16.5 | 3.25 | 19.8 | 6.02 | 1.82 | 5.36 | 3.91 | 1.57 | 1.06 | 0.119 | 4.19 | 142 | 17.6 | 82.4 | 1.00 | 65 | 0.95 | 0.49 |
| Cpx14 | 5.32 | 16.4 | 3.01 | 18.1 | 5.46 | 1.81 | 5.45 | 4.25 | 1.63 | 1.14 | 0.127 | 2.98 | 141 | 17.3 | 77.6 | 1.11 | 63 | 1.00 | 0.49 |
| Cpx23* | 5.37 | 18.3 | 3.45 | 20.7 | 6.26 | 2.01 | 5.57 | 4.52 | 1.88 | 1.14 | 0.129 | 3.93 | 47.0 | 20.0 | 85.6 | 1.22 | 69 | 1.01 | 0.49 |
| Lherzolite | | | | | | | | | | | | | | | | | | | |
| Cpx25 | 4.67 | 14.8 | 2.59 | 15.0 | 4.86 | 1.36 | 4.31 | 3.30 | 1.14 | 0.640 | 0.061 | 2.61 | 135 | 14.7 | 62.4 | 1.09 | 53 | 0.88 | 0.48 |
| Cpx27 | 4.17 | 15.1 | 2.50 | 14.4 | 3.95 | 1.12 | 3.47 | 2.81 | 1.04 | 0.701 | 0.064 | 1.78 | 133 | 14.8 | 60.9 | 1.05 | 49 | 0.90 | 0.53 |
| Cpx32* | 5.07 | 17.0 | 2.94 | 17.1 | 4.71 | 1.50 | 4.65 | 4.37 | 1.52 | 0.832 | 0.033 | 3.23 | 139 | 17.4 | 84.6 | 1.00 | 60 | 0.96 | 0.62 |
| Cpx34 | 3.87 | 14.1 | 2.55 | 13.5 | 3.54 | 1.18 | 3.37 | 2.55 | 1.07 | 0.670 | 0.062 | 1.68 | 134 | 12.1 | 47.4 | 1.13 | 46 | 1.02 | 0.45 |
| Cpx38* | 5.22 | 17.2 | 3.09 | 17.7 | 5.38 | 1.72 | 5.53 | 5.39 | 1.85 | 0.997 | 0.088 | 2.69 | 141 | 17.6 | 83.3 | 0.86 | 64 | 0.95 | 0.56 |
| Cpx30-1r* | 4.36 | 14.3 | 2.48 | 13.9 | 4.54 | 1.40 | 4.03 | 3.55 | 1.29 | 0.690 | 0.054 | 1.08 | 134 | 12.8 | 52.6 | 0.99 | 51 | 0.97 | 0.43 |
| Cpx30-2 | 4.03 | 13.0 | 2.10 | 11.8 | 4.05 | 1.21 | 3.63 | 2.93 | 0.919 | 0.534 | 0.032 | 0.923 | 136 | 11.4 | 40.3 | 0.96 | 44 | 0.94 | 0.38 |
| Cpx30-3 | 3.91 | 12.7 | 2.05 | 11.0 | 3.21 | 1.06 | 3.27 | 2.95 | 0.914 | 0.486 | 0.032 | 1.29 | 135 | 10.8 | 36.5 | 0.80 | 42 | 0.98 | 0.40 |
| Cpx30-4 | 3.87 | 12.6 | 2.28 | 12.6 | 3.88 | 1.19 | 3.24 | 2.66 | 1.12 | 0.573 | 0.046 | 1.32 | 134 | 11.0 | 39.5 | 0.91 | 44 | 0.99 | 0.37 |

[1]r = rim; * = clinopyroxene with sieve texture rather than the clean portion; Cpx 30 is the largest grain; Eu* = $(Sm_{cn} + Gd_{cn})/2$. The HFSE fractionation relative to the REE in cpx can be expressed as the Zr/Zr* ratio, where Zr is chondrite-normalized concentration. Zr* is adapted from the approach of Salters and Shimizu (1988), i.e. Zr* = $((Nd)_{cn}+(Sm)_{cn})/2$. The expression was based on the relative incompatibility of trace elements where Zr is located between Nd and Sm on a compatibility diagram.

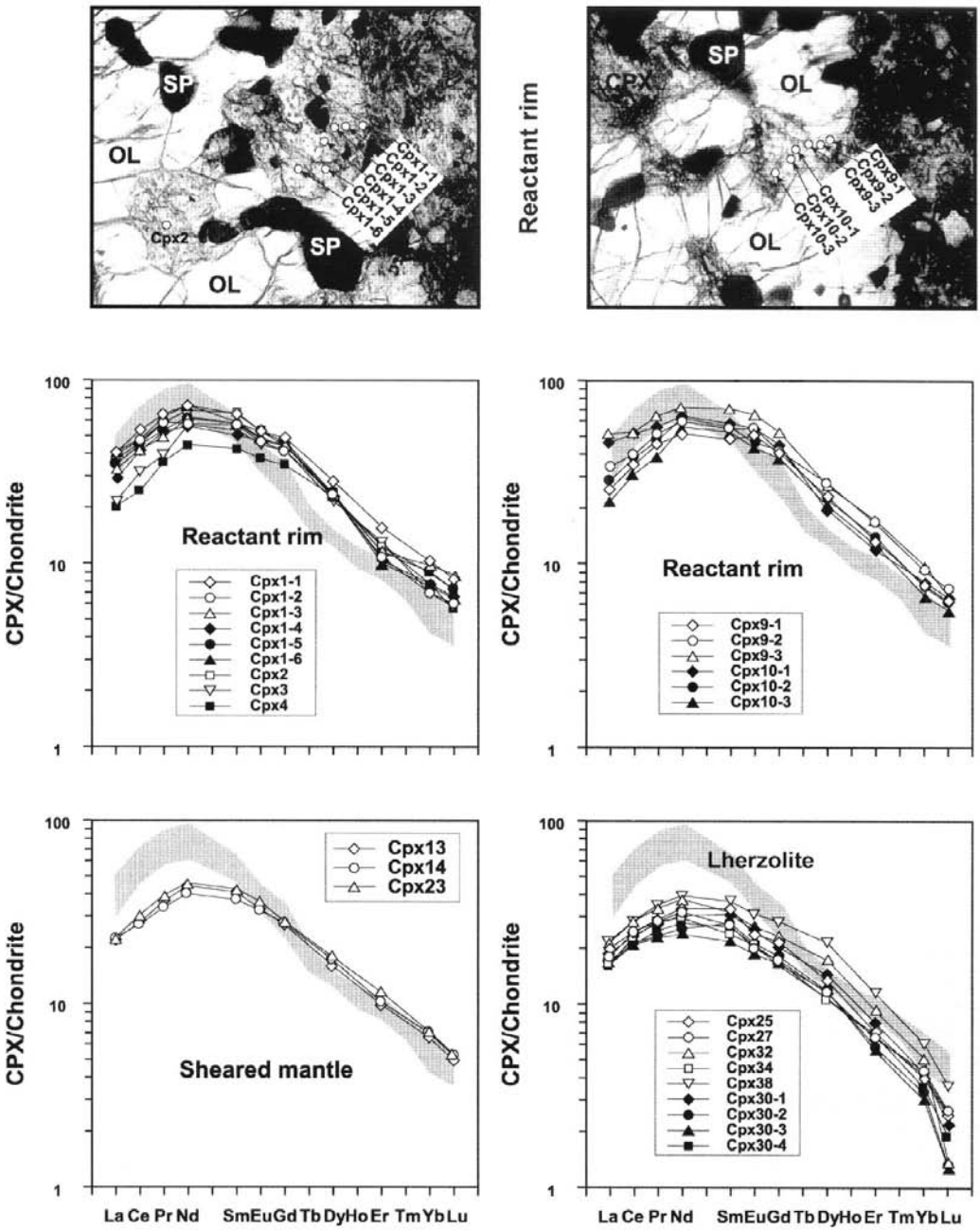



FIG. 8. Chondrite-normalized REE patterns of clinopyroxenes in the composite xenolith. The shaded field shows REE patterns for clinopyroxenes from pyroxenite xenoliths in Fangcheng basalts. Chondrite value is taken from Anders and Grevesse (1989). The photographs in transmitted light show the *in situ* points for SIMS analyses on clinopyroxenes in the reactant rim. The width of the field = 1 mm.

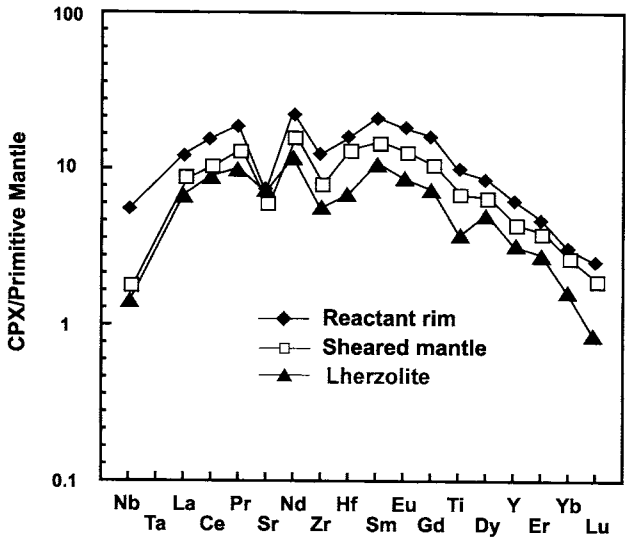



FIG. 9. Primitive mantle–normalized trace element diagrams for the average clinopyroxene compositions of different zones of the composite xenolith. Primitive mantle values are from McDonough and Sun (1995).

(Fig. 8). Low Lu concentrations are similar to the depletion of Lu frequently seen in harzburgite xenoliths worldwide (Downes, 2001).

Clinopyroxenes from the sheared mantle have higher REE (ΣREE = 63–69 ppm) and other incompatible trace element abundances (Table 5 and Fig. 8). Similarly, the metasomatic rim of clinopyroxene (Cpx23) with sieve texture has slightly higher REE, Y, Zr and Nb and lower Sr abundances than the clean core. Clinopyroxenes in the reactant rim generally have higher and more variable trace element abundances (ΣREE = 67–118 ppm) within and between individual grains. Grains (Cpx3 and Cpx4) adjacent to the sheared mantle generally have lower trace element abundances than the grains close to the host basalt (Fig. 8). One important feature is that all the clinopyroxenes in the composite xenoliths show apparent HFSE (i.e., Nb, Zr, Hf, Ti) depletion on primitive mantle–normalized diagrams (Fig. 9 and Table 5), although the degree of depletion increases from the reactant rim to the lherzolite core, especially for Ti (Fig. 9). Sr shows a negative anomaly in all clinopyroxenes of the composite xenolith (Fig. 9).

## Discussion

### *Melt-assisted deformation*

Mantle deformation as revealed by disequilibrating textures and mineral compositions in mantle xenoliths and ultramafic massifs exists in both spinel- and garnet-facies mantle worldwide (e.g., Downes, 1990, 2001; Downes et al., 1992; Klügel, 1998; Zhang et al., 2001a, 2001b, 2003a). Deformation ranges from sheared porphyroclastic (typically with foliation), through recrystallized mosaic (equigranular or tabular) and strongly tectonized, to mylonitized textures, in association with increasing shear strength (Downes, 1990). Deformation generally is accompanied by mineral replacement such as orthopyroxene replacing clinopyroxene, as observed in polymict mantle xenoliths (Zhang et al., 2001a) or as growth of metasomatic minerals such as amphiboles, phlogopites, and Fe-Ti rich minerals (Downes, 1990; Dawson et al., 2001; Zhang et al., 2001b). The fact that sheared peridotites generally show more enriched geochemical characteristics (higher LREE and LILE abundances and enriched Sr and Nd isotopic ratios) than the coexistent granular counterparts (Downes, 1990, 2001; Downes et al., 1992) indicates that deformation and metasomatism are often intricately linked. This is especially true for polymict mantle xenoliths from South Africa (Zhang et al., 2001a, 2001b, 2003a), where the melt ingress led to peridotite-melt interaction and finally considerable changes in trace elemental and oxygen isotopic compositions in minerals (Zhang et al., 2000). Klügel (1998) has also documented the apparent reaction between peridotitic xenolith and host basalt in Canary Islands. All these observations

argue that mantle deformation enhances melt percolation, and vice versa: melt percolation reinforces the deformation.

Large, systematic variations in elemental compositions of minerals from the lherzolite to the reactant rim of the xenolith in this study (Figs. 4A, 5, 6A, 7–8), together with the texture (Figs. 2 and 3), argue for the existence of incipient melt/fluid–assisted deformation in the origin of the composite xenolith. The high percentage of clinopyroxene and olivine and lack of orthopyroxene in the sheared mantle demonstrate that melt-assisted deformation resulted in the dissolution of orthopyroxene and precipitation of clinopyroxene (and olivine). This explains the formation of clinopyroxene with the peculiar texture—i.e., a clean core with a sieve-texture rim (Fig. 3). Good preservation of mineral disequilibrium textures reveals that both melt percolation and deformation happened prior to entrainment of the xenolith into the host magma. Reaction of the xenolith with the melt led to the formation of marked zonation in the reactant rim, as shown by the dramatic drop of MgO in all minerals towards the basalt. High percentages of clinopyroxene and spinel in both the sheared mantle and reactant rim reveal that the infiltration melt responsible for the reaction was calcium and iron rich (i.e., Ca and Fe metasomatism). This is characteristic of shallow-mantle peridotites, as demonstrated by the replacement of orthopyroxene by clinopyroxene and of olivine by monticellite beneath old cratons such as Kaapvaal, Siberia, and Slave (MacKenzie and Canil, 1999; Zhang et al., 2001a). The metasomatic agent was also rich in volatiles such as chlorine.

*Origin of the protolith*

The extreme fertility (Fo <86 in olivine), high opx/cpx ratio, and elemental concentrations in the composite xenolith suggest that its protolith could not be a simple residue of partial melting of primitive mantle and must have been involved in silica-rich melt addition. Indirect evidence of silica-rich melt circulation in lithospheric mantle comes from mass balance calculations and experimental data (Walter, 1998). Kelemen et al. (1992, 1998) found that most mantle xenoliths from the Kaapvaal and Siberian cratons are too high in opx modes (over 30%) to be consistent with a simple restite origin, inasmuch as residues formed by partial melting of primitive mantle at pressures of 25–140 kbar cannot contain more than 23% orthopyroxene. Thus they argued that opx-rich mantle peridotites were modified by the addition of silica-rich melt. However, another possible explanation can be proposed for the origin of this highly fertile xenolith. One may argue that the protolith of the cpx-poor lherzolite was not simply a piece of mantle restite, but was already enriched in orthopyroxene by virtue of the presence of an olivine-bearing orthopyroxenite formed by an earlier stage of melt ingress. In fact this is not the case for the protolith of this cpx-poor lherzolite in this study because of its constituent mineral compositions (Figs. 4B, 6B, and 7). The NiO contents of olivines are similar to those in spinel peridotitic xenoliths from non-cratonic environment and peridotite tectonites worldwide (Walter, 2003; Rudnick et al., 2004). Olivines with low Fo, ranging from 89–90 toward 85, have also been reported for mantle xenoliths from the Shanwang basalts (Wang et al., 1987; Zheng et al., 1998). The olivine compositions in the lherzolite of the present study are distinct from those of low Fo olivines from pyroxenite cumulates (Fig. 4B). The similarity of the lherzolite to non-cratonic peridotitic xenoliths worldwide and the difference from pyroxenitic and peridotitic cumulates worldwide are best shown in clinopyroxene and spinel compositions (Figs. 6B and 7). The much higher $Al_2O_3$ in clinopyroxenes and Cr# in spinels argue strongly against the possibility that the protolith of the lherzolite was of cumulative origin.

Therefore, we consider that the protolith for this composite xenolith was a mantle restite that underwent at least a two-stage processes prior to melt-assisted deformation. The first process, a large degree of polybaric melting, would produce a high Mg#, low opx peridotite residue, and the second process, interaction of the residue with silica-rich melt, would trigger the dissolution of clinopyroxene and olivine and the precipitation of orthopyroxene and the transformation of the protolith to the highly fertile lherzolite. The differences in clinopyroxene REE patterns in the different zones, as well as low HREE abundances in clinopyroxenes of the lherzolite (Table 5 and Fig. 8), require that this melt was different from that which caused the formation of the reactant rim. The extremely low Lu and convex-upward REE patterns either require that the melt responsible for the reaction was derived from a garnet-bearing lithology or reflects depletion of the protolith as a result of partial melting. The melt involved in the reaction may have been derived from crustal materials because clinopyroxenes in the lherzolite have augitic compositions (Fig. 5)

and HFSE depletion (Fig. 9). This feature implies that the lherzolite protolith underwent multiple processes, at least partial melting, a reaction, and interaction with the host magma after entrainment.

This partial melting plus melt-peridotite reaction model can also account for both the magnesium and silica-rich nature of many cratonic peridotites, and the correlation of Ni in olivine with the orthopyroxene mode in cratonic harzburgites (Kelemen et al., 1998; Zheng et al., 1998; Zhang et al., 2001a). Thus, if this model is correct, many Kaapvaal and Siberian harzburgite xenoliths must have been modified by an influx of silica-rich melt. Silica-rich melt circulation in cratonic lithosphere is important for our understanding of cratonic lithospheric evolution, and timing of both calcium-rich and silica-rich melt activities holds vital clues as to how cratonic lithospheric mantle evolves. The preservation of large elemental disequilibria in minerals of the composite xenolith and the textural relationship indicate that the silica-rich melt circulation predated Ca- and Fe-rich melt ingress. The latter must have been related to entrainment of the xenolith, and melt addition made the rock more susceptible to deformation. A period of time at mantle temperature (over 1000°C) would have obliterated the mineral disequilibria to form re-equilibrated textures. Thus, we conclude that silica-rich melt-peridotite interaction was widespread in the Mesozoic lithospheric mantle beneath the North China craton (Zhang, 2005). In summary, the composite xenolith records complicated processes of melt circulation in the mantle.

*Mesozoic lithospheric evolution: Melt-induced transformation*

In the Archean North China craton, the occurrence of high Fo (92–95) olivine xenocrysts and peridotitic xenoliths in Paleozoic kimberlites (Chi and Lu, 1996; Zheng et al., 2001) demonstrates that highly refractory lithospheric mantle indeed existed beneath the craton, similar to the refractory lithospheric mantle beneath other Archean cratons (Boyd, 1989; Boyd et al., 1997; O'Reilly et al., 2001). Moreover, this highly refractory lithospheric mantle could have been preserved at least until the late Paleozoic, inasmuch as no tectonic event or magmatism occurred after the kimberlite eruption. Existence of some high-Mg# peridotitic xenoliths (Zheng et al., 2001) and olivine xenocrysts (Tang et al., 2004) in the Cenozoic basalts reveal that this highly refractory lithospheric mantle was retained beneath some portions of the craton until the Cenozoic. However, these highly refractory mantle peridotites were rare in Upper Cretaceous basalts in the eastern North China craton (Xu et al., 1999; Zhang et al., 2003b; Yan et al., 2003; Ying et al., 2006), except for a few olivine xenocrysts in the Fangcheng basalts (Zhang, 2005). Olivine xenocrysts and peridotitic xenoliths in these Late Cretaceous basalts have Fo less than 92, dominantly in the range of 88–91. In addition, the fact that low Fo (89–92) olivines (Fan et al., 2000; Zheng et al., 2001) are more common in Cenozoic basalt-borne mantle xenoliths in the craton further argues that most highly refractory lithospheric mantle indeed disappeared. Now the question is: How did the highly refractory lithospheric mantle disappear?

Formation of the composite xenolith provides a clue to the answer. As stated above, the composite xenolith records at least two-stage melt-peridotite interaction. In the first stage, silica-rich melt-peridotite reaction triggered by melt ingress could have converted highly refractory peridotite to fertile mantle accompanying precipitation of orthopyroxene (Mg# only 85–86), as shown by the lowest Mg# in the constituent minerals observed in natural samples of mantle xenoliths (Dawson, 1980; Nixon, 1987; Boyd, 1989; Menzies, 1990; Boyd et al., 1997; Gaul et al., 2000; Fan et al., 2000; Zheng et al., 2001; Rudnick et al., 2004). After the reaction, residual melt rich in Ca and Al was possibly trapped to crystallize pyroxenite veins, a typical xenolith suite in Fangcheng basalts (Zhang et al., 2002). Because in a high-temperature environment, rapid elemental diffusion would easily destroy all transient melt processes and elemental disequilibria in the constituent minerals, the chemical re-equilibration would make the melt-peridotite reaction difficult to preserve. This increases difficulties in identification of melt circulation in the lithospheric mantle. Thus, such melt-peridotite reaction might have been more intense than we have observed. Melting of this reconstructed, highly fertile lithospheric mantle in response to lithospheric extension may have resulted in Cretaceous calc-alkaline mafic magmatism (Zhang et al., 2004). This in turn would have led to further thinning of the lithosphere.

In summary, this study suggests that reaction between mantle peridotite and infiltrated melt is an important mechanism for lithospheric evolution, which transformed the lithospheric mantle from a highly refractory to a fertile composition. Consequently, some refractory lithospheric mantle might not be entirely lost as previously believed (Fan and

Menzies, 1992; Menzies et al., 1993) but changed to fertile mantle. The composition of the newly formed lithospheric mantle depends on the composition of the melt involved in the reaction (Kelemen and Ghiorse, 1986; Kelemen et al., 1992; Zhang et al., 2001a). The occurrence of metasomatic harzburgite in many localities worldwide (Kelemen et al., 1992; Zhang et al., 2001a) suggests that this melt-peridotite reaction could be widespread in cratonic lithospheric mantle.

## Conclusions

A highly fertile composite xenolith in Upper Cretaceous basalt records multiple stages of mantle processes involved in their formation. Partial melting was followed by melt percolation during the Mesozoic, which interacted with the refractory peridotite to generate the fertile lherzolite. Melt-assisted deformation enhanced the reaction, which in turn transformed the high-Mg# peridotite to low-Mg# peridotite and changed the lithospheric regime. Deformation also led to the dissolution of orthopyroxene with precipitation of clinopyroxene and olivine. The composite xenolith was in turn affected by the host magma after entrainment, as clearly demonstrated by systematic variations and well-preserved disequilibria in the constituent minerals. Therefore, this composite xenolith records a complex history of lithospheric evolution beneath the southern North China craton.

## Acknowledgments

This research was financially supported by the Chinese Academy of Sciences (KZCX2-YW-103) and the Natural Science Foundation of China (40534022 and 40523003; to H. Zhang), and the Program of Center of Excellence for the 21st Century in Japan (to E. Nakamura). Professors H. Downes and E. R. Neumann are thanked for their constructive comments on an early version of the manuscript.

## REFERENCES

Anders, E., and Grevesse, N., 1989, Abundances of the elements: meteoritic and solar: Geochimica et Cosmochimica Acta, v. 53, p. 197–214.

Boyd, F. R., 1989, Compositional distinction between oceanic and cratonic lithosphere: Earth and Planetary Science Letters, v. 96, p. 15–26.

Boyd, F. R., Pokhilenko, N. P., Pearson, D. G., Mertzman, S. A. Sobolev, N. V., and Finger, L. W., 1997, Composition of the Siberian cratonic mantle: Evidence from Udachnaya peridotite xenoliths: Contributions to Mineralogy and Petrology, v. 128, p. 228–246.

Chi, J. S., and Lu, F. X., 1996, Kimberlites on the North China craton and features of Paleozoic lithospheric mantle: Beijing, China, Science Press (in Chinese).

Chung, S. L., 1999. Trace element and isotope characteristics of Cenozoic basalts around theTanlu fault with implication for the eastern plate boundary between North and South China: Journal of Geology, v. 107, p. 301–312.

Dawson, J. B., 1980. Kimberlites and their xenoliths: Berlin, Germany, Springer Verlag.

Dawson, J. B., Hill, P. G., and Kinny, P. D., 2001, Mineral chemistry of a zircon-bearing, composite, veined and metasomatised upper-mantle peridotite xenolith from kimberlite: Contributions to Mineralogy and Petrology, v. 140, p. 720–733.

Downes, H., 1990, Shear zones in the upper mantle? Relation between geochemical enrichment and deformation in mantle peridotites: Geology, v. 18, p. 374–377.

Downes, H., 2001, Formation and modification of the shallow sub-continental lithospheric mantle: A review of geochemical evidence from ultramafic xenoliths suites and tectonically emplaced ultramafic massifs of western and central Europe: Journal of Petrology, v. 42, p. 233–250.

Downes, H., Embey-Isztin, A., and Thirlwall, M. F., 1992, Petrology and geochemistry of spinel peridotite xenoliths from the western Pannonian Basin (Hungary): Evidence for an association between enrichment and texture in the upper mantle: Contributions to Mineralogy and Petrology, v. 109, p. 340–354.

Fan, W. M., Guo, F., Wang, Y. J., Lin, G., and Zhang, M., 2001, Post-orogenic bimodal volcanism along the Sulu orogenic belt in eastern China: Physics and Chemistry of the Earth (A), v. 26, p. 733–746.

Fan, W. M., Guo, F., Wang, Y. J., and Zhang, M., 2004, Late Mesozoic volcanism in the northern Huaiyang tectono-magmatic belt, central China: Partial melts from a lithospheric mantle with subducted continental crust relicts beneath the Dabie orogen: Chemical Geology, v. 209, p. 27–48.

Fan, W. M., and Menzies M. A., 1992, Destruction of aged lower lithosphere beneath eastern China and accretion of asthenosphere: Geotectonica et Metallogenia, v. 16, p. 171–180 (in Chinese with English abstract).

Fan, W. M., Zhang, H. F., Baker, J., Jarvis, K. E., Mason, P. R. D., and Menzies, M. A., 2000, On and off the North China Craton: Where is the Archaean keel? Journal of Petrology, v. 41, p. 933–950.

Gao, S. Rudnick, R., Carlson, R. W., McDonough, W. F., and Liu, Y. S., 2002, Re-Os evidence for replacement of ancient mantle lithosphere beneath the North China

craton: Earth and Planetary Science Letters, v. 198, p. 307–322.

Gaul, O. F., Griffin, W. L., O'Reilly, S. Y., and Pearson, N. J., 2000, Mapping olivine composition in the lithospheric mantle: Earth and Planetary Science Letters, v. 182, p. 223–235.

Griffin, W. L., Zhang, A. D., O'Reilly, S. Y., and Ryan, C. G., 1998, Phanerozoic evolution of the lithosphere beneath the Sino-Korean Craton, *in* Flower, M. F. J., Chung, S. L., Lo, C. H., and Lee, T. Y., eds., Mantle dynamics and plate interactions in east Asia: American Geophysical Union, Geodynamics Series, v. 27, p. 107–126.

Harris, J. W., Duncan, D. J., Zhang, F., Miao, Q., and Zhu, Y., 1994, The physical characteristics and syngenetic inclusion geochemistry of diamonds from pipe 50, Liaoning Province, People's Republic of China, *in* Meyer, H. O. A., and Leonardos, O. H., eds., Diamonds: Characterization, genesis, and exploration: Brasilia, Brazil, CPRM Special Publication 1/B, p. 105–115.

Han, Z. Z., and Fu, Q., 1993, Genesis of the deep vein and xenolith from Qindao and Zhucheng and its tectonic background: Transactions of Oceanology and Limnology, v. 2, p. 50–58 (in Chinese with an English abstract).

Jordan, T. H., 1975, The continental tectosphere: Review of Geophysics and Space Physics, v. 13, p. 1–12.

Jordan, T. H., 1988, Structure and formation of the continental lithosphere, *in* Menzies, M. A., and Cox, K., eds., Oceanic and continental lithosphere: Similarities and differences: Journal of Petrology, v. Special Lithosphere Issue, p. 11–37.

Kelemen, P. B., Dick, H. J. B., and Quick, J. E., 1992, Formation of harzburgite by pervasive melt/rock reaction in the upper mantle: Nature, v. 358, p. 635–641.

Kelemen, P. B., and Ghiorse, M. S., 1986, Assimilation of peridotite in zoned calc-alkaline plutonic complexes: Evidence from the Big Jim Complex, Washington Cascades: Contributions to Mineralogy and Petrology, v. 94, p. 12–28.

Kelemen, P. B., Hart, S. R., and Bernstein, S., 1998, Silica enrichment in the continental upper mantle via melt/rock reaction: Earth and Planetary Science Letters, v. 164, p. 387–406.

Klügel, A., 1998, Reactions between mantle xenoliths and host magma beneath La Palma (Canary Islands): Constraints on magma ascent rates and crustal reservoirs: Contributions to Mineralogy and Petrology, v. 131, p. 237–257.

Lee, C. T., Yin, Q. Z., Rudnick, R. L., Chesley, J. T., and Jacobsen, S. B., 2000, Osmium isotopic evidence for Mesozoic removal of lithospheric mantle beneath the Sierra Nevada, California: Science, v. 289, p. 1912–1916.

Li, S. G., Xiao, Y. L., Liou, D. L., Chen, Y. Z., Ge, N. J., Zhang, Z. Q., Sun, S. S., Cong, B. L., Zhang, R. Y., Hart, S. R., and Wang, S. S., 1993, Collision of the North China and Yangtze blocks and formation of coesite-bearing eclogites—timing and processes: Chemical Geology, v. 109, p. 89–111.

Li, Z. X., 1994, Collision between the North and South China blocks: A crustal-detachment model for suturing in the region east of the Tanlu fault: Geology, v. 22, p. 739–742.

Liu, J. B., Ye, K., Maruyama, S., Cong, B. L., and Fan, H. R., 2001, Mineral inclusions in zircon from gneisses in the ultrahigh-pressure zone of the Dabie Mountains, China: Journal of Geology, v. 109, p. 523–535.

LSGB (Laboratory of Shandong Geological Bureau), 1981, Geological report: Characteristics for Cenozoic and Mesozoic volcanic rocks within Shandong Province, China: Jinan, China, LSGB, 146 p.

MacKenzie, J. M., and Canil, D., 1999, Composition and thermal evolution of cratonic mantle beneath the central Archaean Slave Province, NWT, Canada: Contributions to Mineralogy and Petrology, v. 134, p. 313–324.

McDonough, W. F., and Sun, S. S., 1995, The composition of the Earth: Chemical Geology, v. 120, p. 223–253.

Meng, Q. R., and Zhang, G. W., 2000, Geologic framework and tectonic evolution of the Qinling orogen, central China: Tectonophysics, v. 323, p. 183–196.

Menzies, M. A., 1990. Continental mantle: Oxford, UK, Clarendon Press.

Menzies, M. A., Fan, W. M., and Zhang, M., 1993, Palaeozoic and Cenozoic lithoprobes and the loss of >120 km of Archaean lithosphere, Sino-Korean craton, China, *in* Prichard, H. M., Alabaster, T., Harris, N. B. W., and Neary, C. R., eds., Magmatic processes and plate tectonics: Geological Society of London Special Publication, v. 76, p. 71–78.

Meyer, H. O. A., Zhang, A., Milledge, H. J., and Mendelssohn, M. J., 1994, Diamonds and inclusions in diamonds from Chinese kimberlites, *in* Meyer, H. O. A., and Leonardos, O. H., eds., Diamonds: Characterization, genesis and exploration: Brasilia, Brazil, CPRM Special Publication 1/B, p. 98–105.

Nakamura, E., and Kushiro, I., 1998, Trace element diffusion in jadeite and diopside melts at high pressures and its geochemical implication: Geochimica et Cosmochimica Acta, v. 62, p. 3151–3160.

Nakamura, E., Makishima, A., Moriguti, T., Kobayashi, K., Sakaguchi, C., Yokoyama, T., Tanaka, R., Kuritani, T., and Takei, H., 2003, Comprehensive geochemical analyses of small amounts (<100 mg) of extraterrestrial samples for the analytical competition related to the sample return mission MUSES-C: Sagamihara, Japan, Institute of Space and Astronautical Science, Report SP 16, p. 49–101.

Nixon, P. H., 1987, Mantle xenoliths. Chichester, UK, John Wiley & Sons Ltd.

Okay, A. I., and Sëngor, A. M. C., 1992, Evidence for continental thrust-related exhumation of the

ultra-high-pressure rocks in China: Geology, v. 20, p. 411–414.

O'Reilly, S. Y., Griffin, W. L., Poudjom Djomani, Y. H., and Morgan, P., 2001, Are lithospheres forever? Tracking changes in sub-continental lithospheric mantle through time: GSA Today, v. 11, no. 4, p. 4–10.

Pearson, D. G., 1999, The age of continental roots: Lithos, v. 48, p. 171–194.

Pearson, D. G., Carlson, R. W., Shirey, S. B., Boyd, F. R., and Nixon, P. H., 1995, Stabilisation of Archaean lithospheric mantle: A Re-Os isotope study of peridotite xenoliths from the Kaapvaal craton: Earth and Planetary Science Letters, v. 134, p. 341–357.

Richardson, S. H., Erlank, A. J., and Hart, S. R., 1985, Kimberlite-borne garnet peridotite xenoliths from old enriched sub-continental lithosphere: Earth and Planetary Science Letters, v. 75, p. 116–128.

Richardson, S. H., Gurney, J. J., Erlank, A. J., and Harris, J. W., 1984. Origin of diamonds in old enriched mantle: Nature, v. 310, p. 198–202.

Riley, T. R., Leat, P. T., Kelley, S. P., Millar, I. L., and Thirlwall, M. F., 2003, Thinning of the Antarctic Peninsula lithosphere through the Mesozoic: Evidence from Middle Jurassic basaltic lavas: Lithos, v. 67, p. 163–179.

Rudnick, R. L., Gao, S., Lin, W. L., Liu, Y. S., and McDonough, W. F., 2004, Petrology and geochemistry of spinel peridotite xenoliths from Hannuoba and Qixia, North China craton: Lithos, v. 77, p. 609–637.

Salters, V. J., M., and Shimizu, N., 1988, World-wide occurrence of HFSE-depleted mantle: Geochimica et Cosmochimica Acta, v. 52, p. 2177–2182.

Sengör, A. M. C., Natal'in, B. A., and Burtman, V. S., 1999, Evolution of the altaid tectonic collage and Palaeozoic crustal growth in Eurasia: Nature, v. 364, p. 299–307.

Tang, Y. J., Zhang, H. F., and Ying, J. F., 2004, High-Mg olivine xenocrysts entrained in Cenozoic basalts in central Taihang Mountains: Relicts of old lithospheric mantle: Acta Petrologica Sinica, v. 20, no. 5, p. 1243–1252 (in Chinese with English abstract).

Walter, M. J., 1998, Melting of garnet peridotite and the origin of komatiite and depleted lithosphere: Journal of Petrology, v. 39, p. 29–60.

Walter, M. J., 2003, Melt extraction and compositional variability in mantle lithosphere, *in* Carlson, R. W., ed., The mantle and core: Washington, DC, Carnegie Institution of Washington, Treatise on Geochemistry, v. 2, p. 363–394.

Wang, F. Z., Jin, L. Y., and Xu, Y. Y., 1987, The study of ultramafic inclusions in Cenozoic basalt in Shandong, Linqu of Shandong: Earth Sciences, v. 12, no. 3, p. 249–256 (in Chinese with English abstract).

Wang, W., and Gasparik, T., 2001, Metasomatic clinopyroxene inclusions in diamonds from the Liaoning province, China: Geochimica et Cosmochimica Acta, v. 65, p. 611–620.

Wang, Y. J., Fan, W. M., Peng, T. P., Zhang, H. F., and Guo, F., 2005, Nature of the Mesozoic lithospheric mantle and tectonic decoupling beneath the Dabie Orogen, Central China: Evidence from $^{40}Ar/^{39}Ar$ geochronology, elemental and Sr-Nd-Pb isotopic compositions of Mesozoic mafic rocks: Chemical Geology, v. 220, p. 165–189.

Wu, F. Y., Walker, R., Ren X. W., Sun D. Y., and Zhou, X. H., 2003, Osmium isotopic constrains on the age of lithospheric mantle beneath northeastern China: Chemical Geology, v. 196, p. 107–129.

Xu, S. T., Okay, A. J., Ji, S., Sengör, A. M. C., Su, W., Liu, Y., and Jiang, L., 1992, Diamond from Dabie Shan metamorphic rocks and its implication for tectonic setting: Science, v. 256, p. 80–82.

Xu, W. L., Zheng, C. Q., and Wang, D. Y., 1999, Discovery of the mantle and lower crust xenoliths in Mesozoic trachybasalts in Liaoxi, China and its significance: Geological Review, v. 45 (suppl.), p. 444–449 (in Chinese).

Xu, Y. G., 2001, Thermo-tectonic destruction of the Archean lithospheric keel beneath the Sino-Korean Craton in China: Evidence, timing, and mechanism: Physics and Chemistry of Earth (A), v. 26, p. 747–757.

Xu, Y. G., Ma, J. L., Huang, X. L., Lizuka, Y., Chung, S. L., Wang, Y. B., and Wu, X. Y., 2004, Early Cretaceous gabbroic complex from Yinan, Shandong Province: Petrogenesis and mantle domains beneath the North China Craton: International Journal of Earth Science, v. 93, p. 1025–1041.

Xu, Y. G., Menzies, M. A., Thirwall, M. F., Huang, X. L., Liu, Y., and Chen, X. M., 2003, "Reactive" harzburgites from Huinan, NE China: Products of the lithosphere-asthenosphere interaction during lithospheric thinning?: Geochimica et Cosmochimica Acta, v. 67, p. 487–505.

Yan, J., Chen, J. F., Xie, Z., and Zhou, T. X., 2003, Mantle xenoliths from Late Cretaceous basalt in eastern Shandong Province: New constraint on the timing of lithospheric thinning in eastern China: Chinese Science Bulletin, v. 48, no. 19, p. 2139–2144.

Yin, A., and Nie, S. Y., 1993, An indentation model for the North and South China collision and the development of the Tan-Lu and Honam fault systems, eastern Asia: Tectonics, v. 12, p. 801–813.

Ying, J. F., Zhou, X. H., and Zhang, H. F., 2004, Geochemical and isotopic investigation of the Laiwu-Zibo carbonatites from western Shandong Province, China and implications for their petrogenesis and enriched mantle source: Lithos, v. 75, p. 413–426.

Ying, J. F., Zhang, H. F., Kita, N., Morishita, Y., and Shimoda, G., 2006, Nature and evolution of Late Cretaceous lithospheric mantle beneath the eastern North China Craton: Constraints from petrology and geochemistry of peridotitic xenoliths from Jünan, Shandong Province, China: Earth and Planetary Science Letters, v. 244, nos. 3-4, p. 622–638.

Zhang, H. F., 2005, Transformation of lithospheric mantle through peridotite-melt reaction: Case of Sino-Korean craton: Earth and Planetary Science Letters, v. 237, p. 768–780.

Zhang, H. F., Mattey, D. P., Grassineau, N., Lowry, D., Brownless, M. Gurney, J. J., and Menzies, M. A., 2000, Recent fluid processes in the Kaapvaal craton, South Africa: Coupled oxygen isotope and trace element disequilibrium in polymict peridotites: Earth and Planetary Science Letters, v. 176, p. 57–72.

Zhang, H. F., Menzies, M. A., Gurney, J., and Zhou, X. H., 2001a, Cratonic peridotites and silica-rich melts: diopside-enstatite relationships in polymict xenoliths, Kaapvaal, South Africa: Geochimica et Cosmochimica Acta, v. 65, p. 3365–3377.

Zhang, H. F., Menzies, M. A., Mattey, D. P., Hinton, R. H., and Gurney, J. J., 2001b, Petrology, Mineralogy and geochemistry of oxide minerals in polymict xenoliths from the Bultfontein kimberlites, South Africa: Implication for low bulk-rock oxygen isotopic ratios: Contributions to Mineralogy and Petrology, v. 141, p. 367–379.

Zhang, H. F., Menzies, M. A., and Mattey, D., 2003a, Mixed mantle provenance: Diverse garnet compositions in polymict peridotites, Kaapvaal craton, South Africa: Earth and Planetary Science Letters, v. 216, no. 3, p. 329–346.

Zhang, H. F., and Sun, M., 2002, Geochemistry of Mesozoic basalts and mafic dikes in southeastern North China craton, and tectonic implications: International Geology Review, v. 44, p. 370–382.

Zhang, H. F., Sun, M., Zhou, X. H., Fan, W. M., Zhai, M. G., and Yin, J. F., 2002, Mesozoic lithosphere destruction beneath the North China Craton: Evidence from major, trace element, and Sr-Nd-Pb isotope studies of Fangcheng basalts: Contributions to Mineralogy and Petrology, v. 144, p. 241–253.

Zhang, H. F., Sun, M., Zhou, M. F., Fan, W. M., Zhou, X. H., and Zhai, M. G., 2004, Highly heterogeneous Late Mesozoic lithospheric mantle beneath the North China Craton: Evidence from Sr-Nd-Pb isotopic systematics of mafic igneous rocks: Geological Magazine, v. 141, p. 55–62.

Zhang, H. F., Sun, M., Zhou, X. H., Zhou, M. F., Fan, W. M., and Zheng, J. P., 2003b, Secular evolution of the lithosphere beneath the eastern North China Craton: Evidence from Mesozoic basalts and high-Mg andesites: Geochimica et Cosmochimica Acta, v. 67, p. 4373–4387.

Zhao, G. C., Wilde, S. A., Cawood, P. A., and Sun, M., 2001, Archean blocks and their boundaries in the North China Craton: Lithological, geochemical, structural, and P-T path constraints and tectonic evolution: Precambrian Research, v. 107, p. 45–73.

Zheng, J. P., O'Reilly, S. Y., Griffin, W. L., Lu, F. X., and Zhang, M., 1998, Nature and evolution of Cenozoic lithospheric mantle beneath Shandong peninsula, Sino-Korean craton: International Geology Review, v. 40, p. 471–499.

Zheng, J. P., O'Reilly, S. Y., Griffin, W. L., Lu, F. X., Zhang, M., and Pearson N. J., 2001, Relict refractory mantle beneath the eastern North China block: Significance for lithosphere evolution: Lithos, v. 57, p. 43–66.